

TITLE

Sex-specific life extension in tauopathy mice by CSF1R inhibition causing selective microglial depletion and suppressed pathogenesis

AUTHORS

Noah R. Johnson^{1,†}, Peng Yuan^{1†}, T. Peter Lopez¹, Weizhou Yue¹, Annalise Bond¹, Brianna M. Rivera¹, Masakazu Hirouchi^{1,2}, Kurt Giles^{1,3}, Atsushi Aoyagi^{1,2}, and Carlo Condello^{1,3, †*}

¹Institute for Neurodegenerative Diseases, UCSF Weill Institute for Neurosciences, University of California, San Francisco, CA 94158.

²Daiichi Sankyo Co., Ltd., Tokyo, 140-8710, Japan.

³Department of Neurology, UCSF Weill Institute for Neurosciences, University of California, San Francisco, CA 94158.

†N.J., P.Y. and C.C. contributed equally to this work. *Correspondence to: carlo.condello@ucsf.edu

ABSTRACT

Microglia are a fundamental component of pathogenesis in many neurological conditions and have specialized functions that vary by disease stage or specific pathology. Drugs targeting colony-stimulating factor-1 receptor (CSF1R) to block microglial proliferation in preclinical disease models have shown mixed outcomes, thus the therapeutic potential of this approach remains unclear. Here, we evaluated CSF1R inhibitors in tauopathy mice using multiple dosing schemes, drug analogs, and longitudinal measurements in the brain and plasma. In both spontaneous disease and in tau fibril inoculation models, we found a region-dependent reduction in insoluble phosphorylated tau and replication-competent tau in mice treated with CSF1R inhibitors. Surprisingly, despite greater drug exposure and microglial depletion in male mice, we observed a rescue of aberrant behavior, reduced plasma neurofilament light chain,

and extended survival in female mice only. Gene expression patterns in CSF1R inhibitor-treated tauopathy mice reverted toward a normal wildtype signature, and *in vivo* imaging revealed suppressed astrogliosis. However, we observed drug dose-dependent upregulation of immediate early genes in male mice only, indicating excitotoxicity, which may have masked functional benefits. Drug-resilient microglia in tauopathy mice exhibited a ramified morphology similar to wildtype microglia but with greater territory occupied per cell, and their transcriptome was neither disease-associated nor homeostatic, suggesting a unique microglial subtype. Our data argue that complete or continuous microglial ablation is neither required nor desired for neuroprotection, and that selective depletion of detrimental, tauopathy-activated microglia may be achieved by precise timing and dosing of CSF1R inhibitors. Importantly, therapeutics targeting microglia must consider sex-dependent effects on functional outcomes when weighing their translational potential for neurological disease.

INTRODUCTION

Microglia, the resident innate immune cells of the central nervous system (CNS), are important for neurodevelopment and homeostasis, and are a fundamental component to pathogenesis in many neurological conditions. We now appreciate that microglia are heterogeneous cells, are influenced by the periphery, have sex-dependent biology, and can be helpful or harmful depending on the disease stage or specific pathology¹⁻⁴. Gene mutations affecting the expression and sequence of microglial genes (e.g. *TREM2*, *CD33*, and *MS4A*) increase risk for Alzheimer's disease (AD), and implicate microglia in several disease pathways including toxic protein aggregation (A β and tau) and neuroinflammation^{5,6}. Thus, for the first time, there is unequivocal evidence in humans that certain microglial functions are robustly involved in the pathogenesis of neurodegenerative disease. However, the precise mechanisms governing microglia function in disease are still not well understood.

In tauopathy (a family of neurodegenerative disorders characterized by tau inclusions in neural cells), there is growing evidence that microglia play an early and constant role in tau aggregation and neuronal loss. Disease-activated microglia assemble an 'inflammasome' protein complex and secrete pro-inflammatory cytokines that regulate neuronal kinases and phosphatases causing tau hyperphosphorylation, aggregation and consequent neurodegeneration⁷⁻⁹. Genome-wide transcriptomic studies have identified innate immune pathways that implicate early and robust involvement of microglia in human tauopathy^{10,11} and

related mouse models¹²⁻¹⁴. Deletion of microglia-specific genes or genetic ablation of microglial cells in rodents have been useful approaches to dissect microglia-mediated mechanisms in disease models, but pharmacologic tools to more dynamically manipulate microglial function have been limited. Recently developed small-molecule drugs targeting colony-stimulating factor-1 receptor (CSF1R), a receptor kinase critical for survival and proliferation of CNS microglia, peripheral tissue macrophages and blood myeloid cells¹⁵, are approved for clinical use in various oncology indications¹⁶, and have now been adopted by the neuroscience community to study microglia biology. In the past few years, there have been numerous studies using CSF1R inhibitors in models of neurological disease, but only a few studies in models of primary tauopathy¹⁷⁻²⁰. While important first steps, these studies only explored single, static time points of treatment, or used only one sex. Given the dynamic nature and complexity of microglial activation, the timing of CSF1R inhibition in tauopathy and its translational relevance is still an open question.

Thus, the goal of our study was to define a therapeutic window that not only reduced pathological markers, but also led to functional improvement. Moreover, we questioned whether complete or continuous microglial ablation using CSF1R inhibitors was necessary given the important and diverse roles these cells play in brain health and disease. Here, we systematically test CSF1R inhibition using multiple drug analogs at several time points in transgenic mice developing spontaneous tauopathy, and in an inoculation model of induced tauopathy. We demonstrate a reduction of tau pathology in multiple dosing schemes without complete microglial ablation; drug exposure levels correlated with the extent of tau-prion²¹ and microglial reduction. Surprisingly, we observed suppressed plasma biomarkers of neurodegeneration, rescue of aberrant behavior, and extended survival in female mice only. These data reveal a previously unrecognized sex-dependent therapeutic benefit of pharmacological CSF1R inhibition. Transcriptome analyses showed that treated tauopathy mice exhibited a restored gene expression profile similar to wildtype mice; however, we observed a specific module of sex- and drug concentration-dependent gene expression that might explain the lack of functional rescue in male mice. Interestingly, residual microglia had a morphology similar to wildtype microglia and their gene expression pattern indicated a unique, homeostatic-like signature that was not responsive to tauopathy nor CSF1R inhibition. These data highlight yet another context for microglial heterogeneity with implications for novel microglial biology, and argue that tempering microglial activation with drugs, rather than cellular ablation, is a better therapeutic strategy with clinical relevance.

RESULTS

CSF1R inhibition reduces pathogenic tau in the brains of Tg2541 mice

Building on previous findings¹⁷⁻²⁰, we first evaluated the effect of CSF1R inhibition on the levels of pathogenic tau in the brains of transgenic mice expressing human tau, using a cell-based tau-prion bioassay, enzyme-linked immunosorbent assay (ELISA), and immunohistochemical (IHC) analysis. Transgenic B6-Tg(Thy1-MAPT*P301S)2541 mice, referred to here as Tg2541 mice, express the 0N4R isoform of human tau with the familial frontotemporal lobar degeneration (FTLD)-linked P301S mutation²², which increases its aggregation propensity and prion-like characteristics^{23,24}. We previously demonstrated that the levels of pathogenic tau in hindbrain regions of Tg2541 mice were greater than in forebrain regions²⁵. Therefore, the forebrain and hindbrain regions were examined separately in this study (Fig. 1a). To deplete microglia, Tg2541 mice were dosed with one of two potent, orally bioavailable, and brain-penetrant CSF1R inhibitors: PLX3397 (pexidartinib), which binds receptor tyrosine kinases CSF1R, and to lesser extent, KIT and FLT3²⁶, and PLX5622, which selectively binds CSF1R²⁷. Three different treatment paradigms were evaluated: acute (2–4 months old), chronic (2–7 months old), and terminal (2 months old until death) (Fig. 1b–d).

We confirmed that CSF1R inhibition effectively reduced microglial markers Iba1 and P2YR12 in both the forebrains and hindbrains of Tg2541 mice compared to vehicle treatment, and that they had similar effects in the brains of C57BL/6J wildtype mice (Supplementary Fig. 1). We found that sex did not have a statistically significant effect for most measures of microglia or pathogenic tau (Supplementary Table 1). Therefore, male and female mice were grouped together for analysis, unless otherwise noted.

We next employed a reproducible and rapid cell-based bioassay^{25,28,29} to measure the activity of replication-competent tau-prions in brain homogenates from Tg2541 mice. To ensure an appropriate dynamic range in this bioassay, we optimized for dilution factor and assay duration using aged Tg2541 mouse brain samples, which showed greater than 100-fold higher signal than wildtype mouse brain samples (Supplementary Fig. 2). Following acute, chronic, or terminal treatment with PLX3397 or PLX5622, tau-prion activity in the forebrains of Tg2541 mice was significantly decreased compared to vehicle-treated mice (Fig. 1e–g).

Hyperphosphorylation and aggregation of tau occurs first in hindbrain regions of Tg2541 mice, especially in the brainstem and spinal cord, leading to motor deficits caused by severe paraparesis²². This is consistent with our previous report of early and aggressive tau-prion

activity in hindbrain regions of Tg2541 mice²⁵; as such, we found that acute CSF1R inhibition was insufficient to reduce tau-prion activity in the hindbrain (Fig. 1e). However, chronic or terminal treatment with PLX3397 did significantly reduce tau-prion activity in hindbrain regions (Fig. 1f,g) and the spinal cords of the Tg2541 mice (Supplementary Fig. 3). To examine other markers of pathogenic tau, we measured the levels of tau phosphorylated at Ser396 (pS396) by ELISA, and tau phosphorylated at Ser202/Thr205 (pS202/T205) by IHC. Acute, chronic, or terminal PLX3397 treatment robustly reduced pS396 tau in both forebrain and hindbrain regions of Tg2541 mice (Fig. 1h–j), and also reduced pS202/T205 tau in forebrain regions (Fig. 1k–m) and in the spinal cord (Supplementary Fig. 3d). Overall, we observed a largely consistent theme of pathogenic tau reduction by CSF1R inhibition, despite a few differences in the therapeutic efficiency of PLX3397 and PLX5622 administered in different treatment paradigms.

Having verified the benefits of microglial depletion at an early disease stage, we next wondered whether initiating CSF1R inhibition at a more advanced stage of disease would have similar effects, simulating an interventional drug treatment. Thus, we dosed Tg2541 mice with PLX3397 in a delayed treatment paradigm (4–7 months old). Similar to terminal treatment, interventional treatment also significantly reduced tau-prion activity in both the forebrain and hindbrain (Supplementary Fig. 4a,b). Although pS396 tau levels were unchanged after interventional treatment, levels of tau phosphorylated at Thr231 (pT231) were reduced in the forebrain (Supplementary Fig. 4c,d). Considering the potential off-target effects of continuous, long-term microglial depletion on brain function, we also wondered whether periodic CSF1R inhibition might provide a safer, yet similarly efficacious therapy. Thus, we also tested PLX3397 dosed intermittently by repeating dosing cycles of three weeks on followed by three weeks off. Intermittent treatment produced similar reductions in the levels of microglial markers in both brain regions as for continuous treatment, but tau-prion activity and pT231 levels were reduced only in the forebrain (Supplementary Fig. 4e–i). Taken together, these data suggest that intermittent/interventional dosing is sufficient to reduce pathogenic tau in the forebrain of Tg2541 mice, likely due to slower disease kinetics; however, continuous CSF1R inhibition is necessary for the extended reduction of pathogenic tau in the hindbrain.

Tau has been shown to propagate throughout the brain in a prion-like fashion along interconnected neural networks^{30–32}. To test the hypothesis that microglial depletion may reduce the propagation of tau-prions²¹ in the brains of Tg2541 mice, we inoculated fibrils of the microtubule-binding repeat domain of tau, referred to as K18 fibrils³³, into the hippocampus and overlying cortex (forebrain regions) of Tg2541 mice and then treated them with PLX3397.

Compared to un-inoculated mice, K18-inoculated mice had significantly increased tau-prion levels in the ipsilateral (inoculated) forebrain, as well as in the contralateral forebrain and in the hindbrain (Supplementary Fig. 5), which suggests that tau-prions had propagated from the inoculation site to those brain regions. However, acute PLX treatment was sufficient to significantly reduce tau-prion levels in the ipsilateral forebrain and hindbrain, as well as in the contralateral forebrain. Furthermore, tau-prion levels in the contralateral forebrain of PLX-treated mice were not significantly different from the forebrain of un-inoculated, vehicle-treated mice (Supplementary Fig. 5), which indicates that CSF1R inhibition prevented the spreading of tau-prions from the inoculation site to this brain region.

CSF1R inhibition can affect peripheral immune cells such as blood myeloid cells and tissue macrophages, in addition to microglia^{18,34}. To determine if the effects of PLX3397 and PLX5622 on pathogenic tau in the brain are due, at least in part, to depletion of peripheral CSF1R-expressing cells we dosed Tg2541 mice with PLX73086, a non-brain penetrant CSF1R inhibitor analog of PLX3397 and PLX5622³⁵. Chronic treatment with PLX73086 had no significant effect on microglial markers Iba1 and P2YR12, or on levels of tau-prions or pTau[S396] or pTau[T231] in the forebrain or hindbrain of Tg2541 mice (Supplementary Fig. 6). Therefore, the effects of CSF1R inhibitors in peripheral compartments do not significantly contribute to their reduction of pathogenic tau in the CNS. Lastly, because there is limited data for CSF1R expression in neurons after injury³⁶, we considered whether PLX3397 or PLX5622 might affect neurons or their expression of tau protein in Tg2541 mice. Acute, chronic, and terminal CSF1R inhibition did not significantly reduce levels of neuronal nuclei (NeuN), detected by IHC, or total tau, detected by ELISA (Supplementary Fig. 7). Therefore, CSF1R inhibitors do not directly affect measures of neuronal viability or tau expression, consistent with a prior report using PLX3397 in cultured primary neurons¹⁸. Together, these data argue that drug effects on biological and functional end points are due to inhibition of CSF1R in CNS microglia.

CSF1R inhibition extends survival and reduces behavioral deficits in female Tg2541 mice

We next focused on the terminal treatment paradigm with PLX3397 to evaluate the long-term effects of CSF1R inhibition on lifespan and behavior. Tg2541 mice develop paraparesis from 5–6 months of age²² which makes feeding difficult, resulting in a loss of body weight and thus, a greatly reduced lifespan compared to wildtype mice. We found that terminal PLX treatment significantly extended the median survival of female Tg2541 mice [16.5 days; $P = 0.0004$], but not male Tg2541 mice, compared to vehicle treatment (Fig. 2a,b). The extended survival in

PLX-treated female mice was preceded by significantly reduced weight loss, which was not observed in male mice (Fig. 2c). Body weight at 180 days of age, irrespective of treatment, was predictive of lifespan in female mice but not in male mice, with less weight loss being correlated with longer survival (Fig. 2d). Lower forebrain tau-prion levels were also correlated with longer survival in female mice but not in male mice (Fig. 2e), suggesting that Tg2541 mice have a sex-specific physiological response to tauopathy. To confirm the effect of PLX treatment on survival in a different experimental paradigm, we used a midbrain inoculation model. Since Tg2541 mice spontaneously develop substantial tau pathology in the midbrain²⁵, we predicted that K18 inoculation in the midbrain would accelerate and synchronize the disease course, which would be ideal for studying mouse survival. Indeed, female Tg2541 mice inoculated with K18 tau fibrils died significantly earlier than mice inoculated with diluent, though no difference was observed in male mice (Supplementary Fig. 8a,b). Consistent with our prior result, PLX treatment significantly extended the median survival of female mice inoculated with K18 tau fibrils [29.5 days; $P = 0.0095$], but not male mice, compared to vehicle treatment (Supplementary Fig. 8c). These data indicate that CSF1R inhibition robustly extends the lifespan of female Tg2541 mice, even during an accelerated disease course.

Previous studies have demonstrated a common hyperactive phenotype in the early stages of tauopathy in transgenic rodent models^{37,38}. While the precise mechanism that leads to this deficit is unclear, this phenotype is causally linked with tau aggregate burden³⁹. Based on the reduction of tau deposition we observed with PLX treatment, we sought to also examine its effect on this hyperactive phenotype. Using an automated home-cage monitoring system, we longitudinally tracked the activity levels in Tg2541 mice at different ages, measuring their amounts of rearing, locomotion, and wheel running. We confirmed previous reports that at early ages the Tg2541 mice displayed a hyperactive phenotype (90–150 days old in females, 90–120 days old in males), while at later ages their activity was significantly reduced (Fig. 2f), likely due to the accumulation of pathogenic tau in brain regions associated with motor function. PLX treatment led to a consistent reduction in Tg2541 mouse hyperactivity, but did not change their hypoactivity at later ages (Fig. 2f), indicating the activity reduction is not due to a general weakening effect. Detailed examination of the individual activity measurements revealed that PLX treatment normalized the amounts of wheel running (Fig. 2g) and active time (Fig. 2h). These data indicate that PLX treatment corrects the aberrant behavior of Tg2541 mice towards that of wildtype mice.

PLX3397 exposure is predictive of disease course in male and female Tg2541 mice

To examine the relationship between drug exposure and markers of disease progression more closely, we collected blood plasma at monthly intervals from mice receiving terminal treatment with PLX3397 or vehicle (Fig. 3a). Consistent with previous reports¹⁸, male Tg2541 mice had higher (25.3%; $P < 0.0001$) plasma concentrations of PLX than female mice (Fig. 3b and Supplementary Fig. 8d); we also observed this difference in wildtype mice (Supplementary Fig. 9a,b). Brain concentrations of PLX were also higher (44.9%; $P = 0.0250$) in male mice (Supplementary Fig. 8e). Male and female mice had *ad libitum* access to food, and had similar rates of food consumption relative to body weight, independent of whether it contained PLX or vehicle (Supplementary Fig. 10a,b). However, female mice were consistently more active than male mice (Supplementary Fig. 10c,d). Thus, the reduced PLX exposure in female mice is likely due to a higher metabolic and drug clearance rate compared with male mice. As only female mice benefitted from PLX, having extended survival and reduced weight loss (Fig. 2b,c), we hypothesize that drug exposure was excessive in male mice, resulting in adverse effects. In line with this hypothesis, we observed a trend towards reduced body weight in male wildtype mice receiving terminal PLX treatment, but not in female wildtype mice (Supplementary Fig. 9c).

Independent of sex, higher plasma concentrations of PLX were correlated with greater microglial depletion in both forebrain and hindbrain regions (Fig. 3c). Furthermore, higher PLX exposure was correlated with reduced tau-prion levels in the forebrain, but not in the hindbrain of Tg2541 mice (Fig. 3d). We also evaluated the plasma levels of neurofilament light chain (NfL), a validated blood-based biomarker of neuronal injury⁴⁰, which correlates with disease progression and tau burden in human tauopathy^{41,42}. Female PLX-treated mice had reduced levels of NfL compared to vehicle-treated mice (Fig. 3e). Conversely, NfL levels were increased in male mice following PLX treatment (Fig. 3f). We found no correlation between NfL level and survival in female mice (Fig. 3g), but in male mice, higher NfL levels were strongly correlated with reduced survival in both PLX and vehicle treatment groups (Fig. 3h). PLX treatment resulted in significantly increased NfL levels in male mice that received midbrain inoculation of K18 tau fibrils, compared to vehicle treatment (Supplementary Fig. 8f,g). Likewise, we found that PLX treatment increased the plasma NfL levels in male wildtype mice (Supplementary Fig. 9d,e), providing additional evidence of CSF1R inhibitor toxicity. Interestingly, intermittent treatment, resulting in a 50% lower total dosage of PLX, produced a significant decrease in NfL levels in male mice (Supplementary Fig. 4j-l). Taken together, these data further confirm that the drug exposure during chronic and terminal treatment with CSF1R inhibitors was appropriate

for female Tg2541 mice to reduce tauopathy and significantly extend survival; however, the drug exposure was too high for male Tg2541 mice and likely resulted in adverse effects such as anemia, leukopenia, and hepatotoxicity, which have been observed in clinical trials⁴³, that outweighed the therapeutic benefit.

CSF1R inhibition shifts gene expression patterns in Tg2541 mice towards wildtype

To better characterize global molecular changes in the CNS due to CSF1R inhibition, we used the Nanostring platform to analyze a curated panel of gene transcripts related to neuroinflammation, myeloid cell function and neuropathology in bulk brain tissue following chronic treatment of Tg2541 mice with PLX5622. We measured mRNA transcripts of 1,841 genes, many of them shown to be regulated by tau or A β pathology in previous genome-wide gene expression studies^{12,14,44}. To validate the Nanostring approach, we identified 53 genes with a broad range of expression level changes and measured mRNA transcripts with quantitative reverse-transcription PCR (RT-qPCR) in the same sample used for sequencing. The RT-qPCR results matched the trends shown in the Nanostring data (Supplementary Fig. 11), indicating that our transcriptomic data was robust.

Since microglial cells are directly impacted by PLX treatment, we first excluded the microglial-specific genes (see Methods) and examined the general trend of expression patterns among different treatment groups. Pearson's correlation matrix showed high similarity among wildtype brains with or without PLX treatment (Fig. 4a), indicating that the gene expression pattern we measured is not affected by the treatment itself. In contrast, PLX treatment in Tg2541 mice caused a distinct shift in the gene expression pattern away from the vehicle-treated group. Interestingly, the correlation coefficients for PLX-treated Tg2541 mice are higher with wildtype mice than with vehicle-treated Tg2541 mice (Fig. 4a dashed boxes and Fig. 4b). To further quantify this shift, we performed partial-least squares (PLS) regression analysis using the gene expression data from vehicle-treated Tg2541 and wildtype mice (Fig. 4c filled circles), and projected the data from PLX-treated mice onto the PLS dimensions (Fig. 4c hollow circles). This allows us to represent the transgene-specific gene expression pattern in a relatively low-dimensional space, and to quantify the changes associated with treatment by calculating the population vector distances and angles in this space. We found that PLX treatment significantly normalized gene expression patterns in Tg2541 mice towards those of wildtype mice (Fig. 4d,e, only two out of five dimensions are shown, covering >95% of the total variance). The normalization in gene expression was further confirmed by similar trends in neuronal-specific

genes (Supplementary Fig. 12). Importantly, PLX treatment in wildtype mice showed negligible changes in the gene expression patterns. These results indicate that PLX treatment specifically suppresses the abnormal transcriptome associated with transgene overexpression, consistent with its effects ameliorating pathogenic tau deposition.

Evidence for excitotoxicity with increased drug exposure

As described above, although we observed consistent reduction in the levels of pathogenic tau in the brains of both male and female Tg2541 mice with PLX treatment (Fig. 1), only female mice benefited from extended survival, functional rescue, and reduced NfL levels (Fig. 2 and Fig. 3). We hypothesize that excessive PLX dosing may underlie this sex-specific effect, as male mice consistently had higher plasma and brain drug concentrations (Fig. 3 and Supplementary Fig. 8), and also benefitted from a lower, intermittent PLX dosing paradigm (Supplementary Fig. 4). Indeed, in our transcriptomics analysis we identified individual genes whose expression was associated with brain PLX concentration or with sex (Fig. 4f). Using a PLS regression of all non-microglia genes to brain PLX concentration and sex for each sample, we calculated the variable importance score along each of these dimensions. Interestingly, many immediate early genes (IEGs) showed high importance scores (Fig. 4g), suggesting that IEGs might be a module that is altered by drug exposure. To further examine this possibility, we examined all immediate early genes^{45,46} (56 genes overlapped in our dataset) and found that their expression patterns fit closely with the brain PLX concentration (Fig. 4h). Importantly, when we excluded the IEGs and examined the PLX-induced transcriptome shift along the WT to TG dimension, the gene expression changes and brain PLX concentration were no longer correlated (Fig. 4i), indicating that the IEGs contribute substantially to the PLX treatment effects. Notably, relative to WT vehicle-treated mice, only male PLX-treated Tg2541 mice had significantly upregulated expression of IEGs (Fig. 4j). As increased IEG expression can be indicative of neuronal hyperactivity, these data provide a plausible mechanism by which excessive PLX dosing may have led to excitotoxicity, thereby masking its therapeutic effect in male mice.

CSF1R inhibition ameliorates pathological activation of astrocytes

As suggested by the reduction of tau deposition, we hypothesized that astrocyte-driven neuroinflammation would also be reduced by PLX treatment. Therefore, we examined transcriptome shifts in astrocyte-specific genes upon PLX treatment. Similar to the neuronal-specific genes, we observed a normalization of astrocyte-specific gene expression patterns

towards WT in both forebrain and hindbrain regions (Fig. 5a, b). In addition, we measured astrogliosis over time using longitudinal bioluminescence imaging (BLI) methods based on a previously established transgenic reporter system of glial fibrillary acidic protein (GFAP)-driven luciferase^{47,48}. To perform reliable BLI in Tg2541 mice, we intercrossed each transgenic line to an albino background and refined the method, using a synthetic luciferin substrate to increase signal from deep hindbrain regions (see Methods and Supplementary Fig. 13). This technique allowed us to non-invasively measure astrogliosis in live mice longitudinally over the course of PLX treatment. In vehicle-treated Tg2541 mice, the BLI signal gradually increased with age, in accordance with the accumulation of tau pathology and gliosis reported in Tg2541 mice^{22,49}. Consistent with our hypothesis, CSF1R inhibition suppressed the BLI signal in both forebrain and hindbrain (Fig. 5c–e), suggesting that astrocytic inflammation driven by microgliosis was attenuated, thus leading to a general neuroprotective effect.

CSF1R inhibition preferentially eliminates a highly activated microglia subpopulation

We next examined the morphological and transcriptional changes in microglia after CSF1R inhibition. In tauopathy, microglia acquire an activated morphology in brain regions where neurons contain tau aggregates (Fig. 6a), a phenomenon seen in many focal neuropathologies^{50,51}. Interestingly, the elimination of microglia in the Tg2541 mouse brain following PLX3397 treatment was not uniform nor complete, but was the most effective in the vicinity of tau aggregates. The microglial density near tau-laden neurons was reduced by more than 60%, but in distal regions (>200 microns) the microglial density was not significantly changed (Fig. 6b), indicating that microglia in the vicinity of the tau aggregates may have increased sensitivity towards CSF1R inhibition. We then compared the morphologies of PLX-resistant (residual microglia in PLX-treated mice) and PLX-sensitive microglia (in vehicle-treated mice). Notably, we found that PLX resistance is associated with more abundant and intricate microglial cell processes, close to the levels seen in wildtype mice (Fig. 6c–f). These data suggest that microglia associated with tau pathology may be in an “activated” state, with a reduced number of processes. This view is consistent with previous reports that activated microglia adopt a “disease-associated microglia” (DAM) phenotype that is pro-inflammatory and detrimental to adjacent neural cells^{13,52}. Interestingly, our data suggests that DAMs are more vulnerable to PLX treatment, and that surviving microglia are less neurotoxic and potentially neuroprotective.

In support of this view, transcriptome analysis showed that many microglial-specific genes were

upregulated in Tg2541 mice (Fig. 7a), among which the most notable were signature DAM genes such as *Tyrobp*, *Clec7a*, *Trem2* and *CD68*. By correlation analysis among different samples using a generalized Louvain algorithm⁵³, we found that the microglia-specific genes in our dataset were clustered into three groups (Fig. 7b and Supplementary Fig. 14). The red-cluster genes showed the highest degree of modulation by transgene overexpression, while the blue-cluster genes showed a moderate degree of modulation, and the green-cluster genes showed almost no difference between Tg2541 and wildtype mice (Fig. 7c). Transgene-modulated genes clustered into red and blue groups, consistent with a recent finding that tau pathology activates both immune-activation and immune-suppression gene expression modules¹⁰. Interestingly, when we compared the gene expression patterns in vehicle- and PLX5622-treated brains, the expression of red- and blue-cluster genes were substantially diminished by PLX, while the green-cluster genes were largely unchanged by the treatment (Fig. 7c). The stability of gene expression in the green cluster is remarkable considering the >50% reduction in microglial cell number. Given that PLX predominantly eliminated microglia in the vicinity of the tau deposits (Fig. 6b), these data suggest that red-cluster genes are preferentially expressed by tau-associated microglia. On the other hand, the lack of changes in green-cluster genes suggests that they are preferentially expressed by the quiescent population of microglia located further away from tau deposition, which are more resistant to PLX-mediated elimination. Moreover, we examined all previously reported DAM signature genes⁵² and we found a partial match with the activation markers in each of our identified gene clusters (Fig. 7d). Regardless of the designation of homeostatic or activation genes reported in previous studies, the red-cluster genes showed a stereotypical pattern of transgene activation and sensitivity to PLX treatment, while green- and blue-cluster genes did not appear to be modulated by these factors. Taken together, our data show morphological and transcriptional changes in microglia associated with tau deposition, consistent with a pattern of pathological activation. CSF1R inhibition appears to preferentially eliminate these microglia, leaving the brain with a more quiescent and less inflammatory microglial population.

DISCUSSION

Our study reveals several major findings from a comprehensive evaluation of CSF1R inhibitors in preclinical models of tauopathy. Importantly, we present the first line of evidence that CSF1R inhibition reduces pathology that leads to functional improvements associated with longer

lifespan in tauopathy mice (Fig. 2 and Supplementary Fig. 8). Overall, our data showing a reduction of pathogenic tau is consistent with prior studies using a different drug scaffold targeting CSF1R (JNJ-527; edicotinib) in Tg2541 mice¹⁹, or using PLX3397 in a different mouse model of tauopathy (TgPS19)¹⁸. However, in our study, neuroprotection occurred despite incomplete microglia depletion (~60%); upon deeper analysis, we identified distinct microglial-specific gene clusters suggesting subsets of microglia responsive to tauopathy or resilient to CSF1R inhibition (Fig. 7). This finding is in line with the wealth of data demonstrating that microglia exist as unique subsets in different brain regions, sexes, ages or disease states²⁻⁴. From this perspective, our data suggest that it may be possible to target specific subsets of activated microglia in tauopathy, while leaving other beneficial microglia alone. Taken together, we argue that CSF1R inhibition causing complete microglia ablation is unnecessary for therapeutic benefits, and may possibly be detrimental in humans given that microglia are important for brain homeostasis and defending against other insults. This notion is at odds with Shi *et al.*, who argue that after PLX3397 treatment, the residual, activated microglia are detrimental¹⁸. This discrepancy could be explained by differences in mouse models such as disease kinetics, the genetic promoter driving the transgene, or the background genetics of the mouse⁵⁴. Another possibility is that Shi *et al.* use a higher drug dose (400 mg/kg) to achieve ~100% microglial ablation, and this may negatively shift the phenotype of residual microglia, or cause concentration-dependent off-target effects on other kinases such as KIT in neurons or PDGFR α in oligodendrocyte precursor cells (OPCs)⁵⁵, leading to reactive microglia. In contrast, a study by Bennett *et al.* showed that partial depletion (~30%) of microglia in Tg4510 mice did not rescue any pathological phenotype²⁰, but PLX3397 was administered to aged mice with advanced pathology, which could explain the negative result, as has been seen in A β models^{56,57}; additionally, Bennett *et al.* used drug formulated in a different chow which may have reduced its exposure and efficacy, as shown previously¹⁸. Furthermore, Tg4510 mice are confounded by genetic factors other than tau causing pathology⁵⁸, thus making it altogether difficult to interpret this data. Nevertheless, these disparate findings in prior literature are now more interpretable alongside our study, which sheds light on the intricate relationships between CSF1R inhibitor dosing, microglial depletion and therapeutic outcomes.

The precise mechanism of CSF1R inhibitors causing reduced tau pathology is still unclear, but our data indicates that activated microglia are the primary target resulting in reduced numbers of cells producing pro-inflammatory cytokines⁷⁻⁹ and other disease-associated microglial factors (Fig. 7) that stoke tau pathogenesis in neurons, such as apolipoprotein E^{18,59,60} and complement

proteins⁶¹⁻⁶³. In addition, it seems plausible that CSF1R inhibitors may also block microglia-mediated activation of astrocytes⁶⁴, which in turn secrete factors that also drive tau pathogenesis; blocking this cellular feed-forward pathway using a different drug targeting microglia led to neuroprotection in a synucleinopathy model of Parkinson's disease⁶⁵. Consistent with this view, PLX-treated mice exhibited a restored astrocyte phenotype (Fig. 5), suggesting that therapeutic benefits in our study may also be due, in part, to quelling disease-associated astrocytes. While there is cross-talk between peripheral immune cells and microglia¹, we show that a non-brain penetrant analog, PLX73086, did not affect CNS microglia or tau pathology (Supplementary Fig. 6), and it is thus unlikely that CSF1R inhibition in the periphery contributes to the phenotypic rescue observed in our study. Lastly, it is possible that chronic PLX treatment caused depletion of some OPCs in our study, but we expect that PLX did not affect mature oligodendrocytes or myelination⁵⁵. The relationship between OPC biology and tau pathology in neurons is largely unknown, and thus it remains unclear how CSF1R inhibition in OPCs contributes, if at all, to the mechanism of action. Nevertheless, this topic warrants further investigation.

Tau pathology in Tg2541 mice is associated with moderate microgliosis and an up-regulation of transcriptomic signatures of microglial activation^{10,13}. Our transcriptome analysis showed activation of two major clusters of microglial-specific genes in Tg2541 mice. These two clusters had a high degree of overlap with the immune activation and suppression modules recently described in tauopathy mice and FTLN patients¹⁰, indicating a specific reactive transcriptional program of microglia towards tau pathology. Consistent with this view, genes in the activated clusters also matched transcriptome modules described in activated microglia in neurodegeneration models (such as *Itgax* and *Clec7a*), but not in tumor or acute inflammation models¹³. We found an additional cluster of microglial genes that had similar expression in Tg2541 and wildtype mice. Intriguingly, this cluster was not affected by PLX treatment, while the other two clusters showed significant down-regulation (Fig. 7). Considering that PLX eliminates more than half of the total microglia population, a parsimonious explanation for this sustained gene cluster is that they are preferentially expressed by an inert microglial subpopulation that does not respond to tauopathy or CSF1R inhibition. Consistent with this notion, we found that PLX treatment preferentially eliminates activated microglia in the vicinity of tau deposits, and thus most surviving microglia are not in direct contact with tau-laden neurons (Fig. 6). This is in contrast to A β mice, in which the surviving microglia are usually associated with A β plaques following PLX treatment^{27,57}. We found that surviving microglia were non-inflammatory, and had

longer and more elaborate processes compared to vehicle-treated microglia, showing functional and morphological features more similar to those of wildtype microglia (Fig. 6). In sum, our data describe a microglial genetic signature that remains stable in Tg2541 mice with or without PLX treatment, likely representing a “dormant” microglial subpopulation that are less dependent on CSF1R for survival, or are less sensitive to CSF1R inhibition at the doses administered in our study.

Sex-specific differences exist in mouse microglial function, gene expression, and response to tauopathy, and the differences increase with age^{60,66,67}. Our data identify a sex-dependent effect on therapeutic exposure and efficacy of CSF1R inhibition in Tg2541 mice. A difference in the plasma levels of PLX3397 during *ad libitum* oral dosing in male and female mice has been noted previously¹⁸; however, only male mice were evaluated further. We examined both male and female Tg2541 mice and found that, despite similar food intake, plasma (and brain) levels of PLX3397 were higher in male mice compared to female mice (Fig. 3 and Supplementary Fig. 8). However, at this level of drug exposure, only female mice received a functional benefit from CSF1R inhibition, an unexpected and clinically relevant outcome that would have been overlooked had our analysis been focused on a single sex. In male Tg2541 mice, despite a robust reduction of microglia and pathogenic tau, PLX treatment did not slow weight loss or extend survival, and plasma NfL levels were significantly increased, indicative of neuronal damage⁴⁰. It has been suggested before that microglia from male animals may exhibit an increased responsiveness to CSF1R depletion compared to microglia from female animals⁶⁸. Our results indicate that despite robust on-target effects for microglial depletion, male mice are more susceptible to toxic off-target effects (on non-microglial cells) of CSF1R inhibitors than previously known. Furthermore, we observed a concentration-dependent activation of IEGs in PLX treated Tg2541 mice, suggesting that excessive PLX dosing in male mice may lead to excitotoxicity (Fig. 4), thus masking the beneficial effect of tau reduction. Curiously, IEGs were not significantly upregulated in male WT mice, indicating that their activation may not be due to high concentration of PLX alone, but may also be dependent on tau deposits. Previous studies have linked tau accumulation and neural activity in vivo⁶⁹. On the other hand, microglia are known to mediate neuroprotection against excitotoxicity^{70,71} and elimination of microglia can exacerbate seizures and related neuronal degeneration⁷². Therefore, the concurrent tau removal and microglial elimination may increase the risk for hyperactivity, resulting in excitotoxicity in male mice with high PLX concentrations. Other sex-specific differences may also contribute to microglial sensitivity to CSF1R inhibition by a currently unknown mechanism.

Future translational studies of pharmacological CSF1R inhibitors will need to carefully evaluate the role of sex in both safety and therapeutic outcomes.

CSF1R inhibitors were shown to be protective in mouse models of other neurodegenerative diseases, such as AD and Down syndrome^{27,73-75}. However, under different treatment conditions, CSF1R inhibition did not affect A β plaque burden, but did rescue some functional deficits^{56,57}. Therefore, microglia play a dynamic role in the brain's response to A β pathogenesis, and their attenuation may impart distinct benefits at different stages of disease. Our results suggest that, in primary human tauopathies, a subset of microglia play a net negative role before, during, and after disease onset and that their removal may be a viable therapeutic strategy. It remains to be determined if similar benefits should be expected for tauopathy in AD given the preceding comorbid A β pathology, but this may be elucidated in rodent models co-expressing human tau and A β . Nevertheless, because CSF1R inhibition has not been reported to be detrimental in A β mice, CSF1R inhibitors could ameliorate AD-related tauopathy even if caused by different disease mechanisms. Ongoing human clinical trials of CSF1R inhibitors in AD (e.g. NCT04121208) may provide additional mechanistic insights.

Primary human tauopathies constitute a class of neurodegenerative diseases caused by tau misfolding and aggregation and include progressive supranuclear palsy (PSP), corticobasal degeneration (CBD) and Pick's disease, among others⁷⁶. When combined with AD, in which tau aggregation follows A β deposition, tauopathies afflict a significant proportion of the human population, and thus novel approaches to directly or indirectly block tau pathogenesis or its downstream effects are urgently needed. Our study highlights several aspects of pharmacological CSF1R inhibition that bolster its therapeutic potential for human tauopathies. First, we demonstrated that interventional dosing of Tg2541 mice, initiated at a stage when robust tau deposition had already occurred^{22,25}, led to a significant reduction in pathogenic tau (Supplementary Fig. 4). Therefore, our data support the clinical benefit of CSF1R inhibitors for both treatment, and prevention, of tauopathy. This is important because prophylactic treatment of non-autosomal dominant neurodegenerative diseases is difficult due to a lack of definitive prognostic biomarkers paired with the fact that aggregation of the causative proteins can occur years or decades prior to symptom onset^{29,77}. Second, we found that intermittent dosing of Tg2541 mice at three-week intervals produced a significant reduction in pathogenic tau (Supplementary Fig. 4). Despite relatively minimal off-target effects from continuous, long-term dosing of CSF1R inhibitors in mice²⁷, non-human primates⁷⁸, and humans^{26,79}, intermittent dosing would be clinically preferable if a similar therapeutic outcome was achieved, given the

important functions for microglia and related peripheral cells in innate immunity. Because neurodegenerative tauopathies are slow, protracted diseases and microglia are long-lived⁸⁰, it is conceivable that breaks in dosing may occur on the order of months or years and be informed by medical imaging probes for microglia activation⁸¹. Third, we found CSF1R inhibition to extend the survival of female Tg2541 mice (Fig. 2 and Supplementary Fig. 8), indicating that the reduction in pathogenic tau in this model system translates to an improved clinically relevant outcome. We postulate that if CSF1R inhibitor dosing was optimized for male Tg2541 mice, any adverse effects in the CNS or periphery would likely be diminished and their survival extended. Fourth, we showed that complete microglial depletion is not necessary, or even desirable, for a therapeutic benefit. As discussed above, the microglia that survive CSF1R inhibition represent a unique microglial sub-population that likely serves important functions in brain homeostasis. Future preclinical studies may pinpoint the precise level, timing, and frequency of CSF1R inhibition such that the detrimental effects of microglial activation are minimized while an appropriate number of homeostatic microglia remain for brain surveillance. Lastly, CSF1R inhibitors applied in conjunction with tau immunotherapy^{82,83} may prove to be a successful combination therapy; because microglia are not needed for antibody effector function⁸⁴, removing tauopathy-activated microglia would slow tau pathogenesis and may also increase the efficacy of tau immunotherapy. Taken together, our data strongly support the therapeutic modulation of microglial activation by CSF1R inhibitors as a promising approach to treating human tauopathies.

METHODS

Animals

The Tg2541 transgenic mouse line expresses the human 0N4R tau isoform under the Thy1.2 genetic promoter. Tg2541 mice were originally generated on a mixed C57BL/6J × CBA/Ca background²² and were then bred onto a congenic C57BL/6J background using marker-assisted backcrossing for eight generations before intercrossing to generate homozygous mice. Albino Tg2541 mice were generated by intercrossing Tg2541 with C57BL/6J mice expressing a spontaneous mutation in the tyrosinase gene (homozygous for Tyr^{c-2J}) causing albinism (Jackson Laboratory; 000058). To generate mice for *in vivo* bioluminescence imaging, we employed Tg(*Gfap-luc*) mice, which express firefly luciferase under the control of the murine *Gfap* promoter (gift from Caliper Life Sciences). These reporter mice were originally on the FVB

background, but we backcrossed them to a congenic B6 background, and then crossed them to the B6-albino background. To create bigenic mice, albino Tg2541 mice were crossed with albino Tg(*Gfap-luc*) animals to produce double hemizygotes; next, double hemizygotes were crossed and the progeny were screened for the presence of both transgenes expressed at homozygosity. Animals were maintained in a facility accredited by the Association for Assessment and Accreditation of Laboratory Animal Care International in accordance with the *Guide for the Care and Use of Laboratory Animals*. All procedures for animal use were approved by the University of California, San Francisco's Institutional Animal Care and Use Committee.

PLX compound formulation in mouse chow

PLX3397 was provided by Plexxikon Inc. and was formulated in AIN-76A standard chow by Research Diets Inc. at 275 mg/kg as previously described⁸⁵. PLX5622 was provided by Plexxikon Inc. and was formulated in AIN-76A standard chow by Research Diets Inc. at 1200 mg/kg as previously described⁵⁷. PLX73086 was provided by Plexxikon Inc. and was formulated in AIN-76A standard chow by Research Diets Inc. at 200 mg/kg as recommended by Plexxikon Inc.

Immunohistochemistry and slide scanning

Formalin-fixed samples were embedded into paraffin using standard procedures and microtome-cut into 8 μ m sagittal brain sections or coronal spinal cord sections and mounted onto slides. To reduce tissue autofluorescence, paraffin slides were photobleached for 48 hours⁸⁶. Slides were deparaffinized in a 61°C oven for 15 minutes and rehydrated through alcohols. Antigen retrieval was performed by autoclaving for 10 minutes at 121°C in 0.01 M citrate buffer. Sections were blocked in 10% normal goat serum (NGS) (Vector Labs) for 1 hour at room temperature. All primary antibodies were used at 1:250 dilution and included rabbit monoclonal anti-Iba1 (Abcam, ab178847), rabbit polyclonal anti-P2YR12 (Atlas, HPA014518), mouse monoclonal anti-NeuN (Millipore, MAB377), and mouse monoclonal anti-pS202/T205 tau (AT8; Thermo Fisher, MN1020). Primary antibodies were diluted in 10% NGS in PBS and allowed to incubate on the slides overnight at room temperature. Primary antibody detection was performed using goat secondary antibodies with conjugated AlexaFluor 488, AlexaFluor 555, or AlexaFluor 647 (Life Technologies) at 1:500 dilution. Slides were cover-slipped using PermaFluor mounting medium (Thermo). Whole-section tiled images were acquired with an Axioscan.Z1 slide scanner (Zeiss) at 20 \times magnification, and quantification was performed with

Zen 2.3 software (Zeiss).

Cellular bioassay to measure tau-prion activity

A HEK293T cell line expressing the repeat domain of 4R human tau (aa 243–375) containing the P301L and V337M mutations and C-terminally fused to YFP was previously generated as described^{28,87}. A stable monoclonal line was maintained in DMEM, supplemented with 10% FBS and 1% penicillin/streptomycin. To perform the bioassay, 3,000 cells (containing 0.1 µg/ml Hoechst 33342) were plated in 70 µl per well into 384-well plates (Greiner) and incubated for 2 hours before treatment with samples. Clarified brain lysate at a final concentration of 1.25 µg/mL total protein was first incubated with Lipofectamine 2000 (0.2% final concentration) and OptiMEM (9.8% final concentration) for 90 minutes, and then added to the plated cells in quadruplicate. Plates were incubated at 37°C for 1–3 days, and then the live cells were imaged using an INCell Analyzer 6000 Cell Imaging System (GE Healthcare) and custom algorithms were used to detect fluorescent YFP-positive puncta (aggregates).

Mechanical tissue homogenization

Postmortem brains and spinal cords were thawed and weighed to determine the mass in grams. Brains were bisected into forebrain and hindbrain pieces using a single cut with a scalpel blade between the striatum and hypothalamus. Tissue was homogenized in nine volumes of cold DPBS containing Halt Protease Inhibitor Cocktail (1x, Thermo Fisher Scientific) using a Precellys 24-bead beater (Bertin Instruments) with metal bead lysing matrix (MP Biomedical). Where necessary, brain lysates were clarified by centrifugation at 10,000 × g for 10 min at 4°C. All tissue and samples were stored at –80°C until further use.

Formic acid extraction of insoluble proteins in brain tissue for ELISA

Fifty microliters of formic acid were added to 25 µL of 10% brain homogenate and placed in an ultracentrifuge tube. The samples were vortexed, sonicated for 20 minutes at 37°C in a water-bath sonicator, and then centrifuged at 100,000 × g for 1 hour. Fifty microliters of supernatant were recovered to a low-binding tube and neutralized with 950 µL of neutralization buffer (1 M Tris base and 500 mM dibasic sodium phosphate). Samples were aliquoted into low-binding tubes and flash frozen in liquid nitrogen. The following ELISA kits from Thermo Fisher Scientific were used according to the manufacturer's protocols: total tau (KHB0041), p-tau S396 (KHB7031), and p-tau T231 (KHB8051). Each sample was analyzed in duplicate. Raw ELISA values were adjusted to total brain protein (grams) in the clarified 10% brain homogenate as

determined by bicinchoninic acid (BCA) assay (Pierce/Thermo Fisher Scientific).

Quantification of total protein in brain homogenate

Total protein content in the PBS-soluble (clarified 10% brain homogenate) and detergent-soluble fractions was quantified using the Pierce BCA Protein Assay Kit (Thermo Fisher Scientific) following the manufacturer's protocol.

Generation of tau K18*P301L fibrils

Production, purification and fibrillization of recombinant tau K18*P301L fibrils were performed as previously described⁸⁸.

Stereotaxic injections in Tg2541 mice

Forebrain inoculation: Ten-week-old Tg2541 mice received unilateral inoculations of 10 μ l of 1.5 mg/ml tau K18 P301L fibrils using stereotaxic methods. Injections followed a two-step process: the needle was first advanced to the hippocampus (Bregma -2.5mm, Lateral 2.0mm; Depth -2.3 mm from the skull surface) to deliver 5 μ l over three minutes, then the Hamilton syringe pump was paused for five minutes to allow for diffusion prior to retracting the needle to the overlying cortex (Depth -1.3 mm) where the remaining 5 μ l was injected. After fibril injection, the needle remained in place for five minutes to allow for diffusion of fibrils before retraction, patching the skull and suturing the scalp. Midbrain inoculation: Ten-week old Tg2541 mice received bi-lateral inoculations of 10 μ l of 1.5 mg/ml tau K18 P301L fibrils using stereotaxic methods. Five microliters was injected at each site in the midbrain (Bregma, -4.3 mm; Lateral, 1.0 mm, Depth, -2.5 mm) and (Bregma, -4.3 mm; Lateral, -1.0 mm, Depth, -2.5 mm).

Automated home cage monitoring of behavior

Total activity measurements of freely moving mice were made every 30 days after PLX dosing in Promethion cages (Sable Systems International). At each time point, mice were first randomized and placed individually in Promethion cages for 4 to 6 days. Real-time cage activity recording was continuous during the entire session using a combination of a running wheel with sensors to measure speed and distance traveled, three balances to measure body weight, food and water consumption, and a matrix of infrared light beams to measure XYZ movements with 0.25 cm resolution. Analysis of these metrics was used to detect behaviors such as sleep, rearing and general locomotion. For each mouse, data used for analyses were average readings per light or dark cycle. Data from the first circadian cycle were excluded due to variable

behavior during habituation. To calculate the activity scores, wheel use, locomotion and rearing were first normalized to a 0–1 scale by the maximum value in the whole dataset, and then the geometric mean of the normalized values for each session was calculated.

Quantification of PLX compound levels in brain tissue and plasma

Brain homogenates (20% w/v) were prepared in PBS by one 30-second cycle of bead beating at 5500 rpm with a Precellys 24-bead beater (Bertin Instruments) or plasma samples were prepared by dilution to 25% with PBS. Compounds were recovered by mixing equal parts of brain homogenate with a 50/50 (v/v) solution of acetonitrile (ACN) and methanol containing 1 mM niflumic acid. Precipitated proteins were removed by vacuum filtration (Captiva ND, Agilent). Analysis was performed using a liquid chromatography-tandem mass spectrometry system consisting of an API4500 triple quadra-pole instrument (AB Sciex, Foster City, CA) interfaced with a CBM-20A controller, LC20AD 230 pumps, and a SIL-5000 auto-sampler (Shimadzu Scientific, Columbia, MD). Samples were injected onto a BDS Hypersil C8 column maintained at room temperature. The amount of ACN in the gradient was increased from 75–95% ACN over two minutes, held for one minute, and then re-equilibrated to 75% ACN over 1.4 minutes. Data acquisition used multiple reaction monitoring in the positive ion mode. Specific methods were developed for each compound (PLX3397 and PLX5622), enabling the determination of absolute concentrations.

Blood plasma neurofilament light (NfL) protein measurement using SIMOA

At monthly time points, 150 μ l blood was collected in EDTA-coated tubes. The plasma was centrifuged at 1,000 x g for ten minutes to clarify the samples, and was then diluted with sample diluent buffer included in the kit by 25-fold and 100-fold, respectively, prior to the measurement. Plasma NfL concentration was measured and analyzed using the NfL kit (Quanterix) with the SIMOA HD-1 analyzer (Quanterix). Briefly, samples, magnetic beads coated with capture antibody, and biotinylated detector antibodies were combined. Thereafter, the capture beads were resuspended with streptavidin- β -galactosidase (SBG) and resorufin β -D-galactopyranoside (RGP) and transferred to the SIMOA disk. Each bead fit into a microwell in the disk and if NfL was captured then the SBG hydrolysed the RGP substrate which generated a fluorescent signal, and then the concentration was measured against a standard curve derived from known concentrations of recombinant NfL included in the kit. The lower limit of quantification of the assay for plasma was 17.15 pg/mL.

RNA extraction and Nanostring RNA expression measurements

RNA later-preserved samples were homogenized in PBS and total RNA was extracted from samples using the Quick-RNA Miniprep Kit (Zymo Research). RNA extracts were evaluated for concentration and purity using a Nanodrop 8000 instrument (Thermo Fisher Scientific) and diluted to a concentration of 20 ng/ μ l. Hybridizations were performed for the mouse Neuroinflammation, Myeloid cell, and Neuropathology panels according to the nCounter XT Assay user manual (Nanostring). The hybridizations were incubated at 65°C for 16 hours, and then were added to the nCounter SPRINT Cartridge for data collection using the nCounter SPRINT Profiler. Counts were analyzed using the nSolver Analysis Software.

RNA expression analysis

In total, there were 10 mice in the Tg2541 vehicle group, 10 mice in the Tg2541 PLX5622 group, 6 mice in the wildtype vehicle group, and 6 mice in the wildtype PLX5622 group. Each mouse had separate forebrain and hindbrain samples and three panels of Nanostring sequencing were performed on each sample. Data from the three panels were pooled together to form the final dataset. When pooling data, if a gene appeared in more than one panel then the average read value was used in subsequent analysis, unless one panel failed to detect the gene.

To assign cell-type specificity of each gene, we used the transcriptome dataset reported in a previous study⁸⁹, inspired by previously reported approaches in bulk tissue samples¹³. We set a specificity threshold in which a gene qualifies to be cell-type specific if its expression in a cell type is greater than five times the sum in all other cell types. Using this standard, our dataset had 242 microglia-specific genes, 47 astrocyte-specific genes and 70 neuron-specific genes. All cell-type specific gene analyses were repeated with a three-time threshold and all results were consistent (data not shown).

We used partial least-square (PLS) regression (MATLAB) to extract the gene expression pattern aligned with Tg2541-wildtype axis, using individual gene reads from each mouse as predictors and genotype as responses. Only vehicle groups were used in constructing the PLS regression. Forebrain and hindbrain were calculated separately. Five output dimensions were chosen for all PLS analyses, as they covered 99.99% of the total variance in all cases. The scores in the first two dimensions were plotted. To project PLX3397-treated groups to the PLS dimensions, we used the following formula:

$$Score_{projection} = (Loading_{predictor} \setminus (raw - mean_{predictor}))'$$

To calculate population vector distance, we use the “mhal” command in MATLAB. All five dimensions were used for each mouse. The wildtype vehicle group was used as a target.

To calculate the vector angle, each mouse’s gene expression pattern was regarded as a five-dimension vector in the PLS space, and the angle between each mouse and the average vector of the wildtype vehicle group was calculated with the following formula:

$$A = \cos^{-1}((u \cdot v)/(|u||v|))$$

To calculate the PLS regression along the PLX concentration and sex-correlated dimensions, we constructed regressions using all non-microglial genes or only immediate early genes⁴⁵ to measured brain PLX concentrations and sex of each sample. We then calculated variable importance in projection to isolate the genes important for the regression. To calculate the projected PLX concentrations, we used the products of gene expression levels and coefficients estimated from PLS regression.

To calculate clusters in the microglial-specific genes, we calculated pairwise Pearson’s correlation coefficients across 32 samples among each gene. The resulting similarity matrix was then processed with a generalized Louvain community detection algorithm⁵³.

Gene expression analysis by RT-qPCR

Mouse brains were collected at endpoints and flash frozen in DNA/RNA shield reagent. Tissue was homogenized as described above and total RNA was purified using a commercial isolation kit (Zymo Research). RNA concentration and the RNA integrity number (RIN) were determined using a Bioanalyzer 2100 instrument and an Agilent RNA 6000 Pico Kit (Agilent 5067-1513). Only samples with a RIN score ≥ 7.0 were used for gene expression analysis. To confirm transcriptome profiling results, 2.5 ng of sample mRNA was applied to triplicate RT-qPCR reactions consisting of 1x TaqPath 1-Step Multiplex Master Mix (ThermoFisher Scientific A28526), Taqman primer/probe sets and a normalizing human MAPT Taqman assay. Reactions were run on a QuantStudio 6 and 7 Pro instrument and amplification yielding cycle threshold (C_T) values were corrected with Mustang Purple passive reference dye for each target gene. Gene expression of PLX-treated mice relative to vehicle-treated mice was determined by the comparative C_T method and values were expressed as fold-change⁹⁰.

Comparative C_T equation:

$2-\Delta\Delta C_T = [(C_T \text{ gene of interest} - C_T \text{ hMAPT internal control})_{\text{PLX-treated mice}} - [(C_T \text{ gene of interest} - C_T \text{ hMAPT internal control})_{\text{vehicle-treated mice}}]$

In vivo bioluminescence imaging

Bioluminescence imaging was performed on the brains and spinal cords of albino bigenic Tg(2541:*Gfap-luc*) homozygous mice after receiving an intraperitoneal injection of 25 mg/kg cyclic luciferin-1 (CycLuc1) sodium salt solution (Aobious; AOB6377) prepared in PBS, pH 7.4. After CycLuc1 injection, mice were placed in an anesthetization chamber and exposed to an isoflurane/oxygen gas mix for ten minutes. During this time, the heads of the mice were shaved to enhance the bioluminescence signal. After anesthetization, mice were placed in an IVIS Lumina III small animal imaging system (PerkinElmer) and were kept under constant anesthesia. Mice were imaged for 60 s duration at three time points (14, 16 and 18 minutes) following CycLuc1 injection as determined in one-hour time-lapse calibration studies. After image acquisition, the mice were allowed to recover in their home cages. Brain and spinal cord bioluminescence values were calculated from images displaying surface radiance using standardized regions of interest and were then converted to total photon flux (photons per second) using Living Image software version 4.4 (PerkinElmer).

Confocal imaging of thick tissue sections

Vibratome-sectioned brain slices (40 μm thick) were immunolabeled with Iba1 and AT8 antibodies using standard protocols for free-floating sections in multi-well plates. Sections were mounted using PermaFluor and #1.5 coverglass. Using a Leica SP8 confocal microscope equipped with HyD detectors and an AOBS, samples were first visualized using Navigator function to acquire an overview image of each slice using a 20x water-immersion lens (0.95 NA). From the mosaic image, smaller tiled-ROIs were marked in the forebrain and hindbrain to acquire high-resolution, sequential-scanned image stacks using a 63x water-immersion lens (1.2 NA). Eight-bit image z-stacks (1 μm steps) were collected at 512x512-pixel resolution. Images were processed using custom MATLAB code.

Microglial morphology analysis

Microglia morphology was analyzed using a custom script in MATLAB. Briefly, raw confocal image stacks were smoothed and then maximally projected. Isolated microglia cells were manually selected for analysis. The selected microglia region was binarized with an intensity threshold, and then the cell body was detected by fitting a largest circle in the binary mask. After

excluding the cell body region, the remaining microglia processes were skeletonized and branch number, branch length and bounding box were measured using “regionprops” and “bwmorph” commands.

Statistical analysis

All statistical analyses were performed using GraphPad Prism 8. Comparisons between two groups were performed by two-tailed unpaired t test or by Mann-Whitney nonparametric test. For comparisons of more than two groups, one-, two-, or three-way ANOVA was performed with Holm-Šidák post hoc analysis. Following ANOVA, residuals were evaluated for normal distribution using the Anderson-Darling test and the data were evaluated for equal variance using the Brown-Forsythe test. If both assumptions were violated ($P < 0.05$), the data was reanalyzed using Welch’s ANOVA with Dunnett T3 post hoc analysis. For repeated-measures ANOVA, sphericity was not assumed and the Geisser-Greenhouse correction was applied. If any data points were missing, a mixed-effects model (Restricted maximum likelihood; REML) was used instead. Pearson’s correlation tests were performed as one-tailed tests as, in each case, we had a directional hypothesis of either positive or negative correlation. Sample sizes are shown in graphs with each data point representing an individual mouse, or are reported in the figure legends. Experimental replication and exact statistical tests used are detailed in the figure legends.

ACKNOWLEDGEMENTS

We thank Plexxikon, Inc for providing the PLX3977, PLX5622 and PLX73086 compounds, and Andrey Reymar and Brian West for consulting on drug dosing and chow formulation. We thank Julian Castaneda, Karina Walker and Lyn Batia (and their staff) at the UCSF Hunter’s Point animal facility for coordinating transgenic mouse development, breeding, and drug efficacy studies. We thank Masahiro Inoue (Daiichi Sankyo, Inc.) for insightful discussions on pharmacokinetics and pharmacodynamics in our study. We thank Stanley Prusiner and David Ramsay at the UCSF Institute for Neurodegenerative Diseases (IND) for access to equipment and technical resources critical for the completion of this study. We thank the following UCSF IND staff for technical assistance: Abby Oehler, Rigoberto Roman-Albarran, Julia Becker, Marta Gavidia and Manuel Elepano. The study was funded by grants from the National Institutes of Health (NIH): (# RF1 AG061874 and P01 AG002132), as well as by the Rainwater Charitable

Foundation, the Sherman Fairchild Foundation, and Daiichi Sankyo, Inc. Competing interests: The Institute for Neurodegenerative Diseases (UCSF) had a research collaboration with Daiichi Sankyo, Inc. (Tokyo, Japan).

AUTHOR CONTRIBUTIONS

C.C. conceived the study and designed experiments. N.J., T.P.L., W.Y., A.B., B.M.R., H.M., K.G., A.A., and C.C. performed experiments and prepared data. N.J., P.Y., and C.C. analyzed and interpreted data. N.J., P.Y., and C.C. wrote the paper. C.C. supervised the study.

REFERENCES

1. Dionisio-Santos, D.A., Olschowka, J.A. & O'Banion, M.K. Exploiting microglial and peripheral immune cell crosstalk to treat Alzheimer's disease. *J Neuroinflammation* **16**, 74 (2019).
2. Masuda, T., *et al.* Spatial and temporal heterogeneity of mouse and human microglia at single-cell resolution. *Nature* **566**, 388-392 (2019).
3. Kodama, L. & Gan, L. Do Microglial Sex Differences Contribute to Sex Differences in Neurodegenerative Diseases? *Trends Mol Med* **25**, 741-749 (2019).
4. Stratoulis, V., Venero, J.L., Tremblay, M.E. & Joseph, B. Microglial subtypes: diversity within the microglial community. *EMBO J* **38**, e101997 (2019).
5. Schwabe, T., Srinivasan, K. & Rhinn, H. Shifting paradigms: The central role of microglia in Alzheimer's disease. *Neurobiol Dis* **143**, 104962 (2020).
6. Shi, Y. & Holtzman, D.M. Interplay between innate immunity and Alzheimer disease: APOE and TREM2 in the spotlight. *Nat Rev Immunol* **18**, 759-772 (2018).
7. Maphis, N., *et al.* Reactive microglia drive tau pathology and contribute to the spreading of pathological tau in the brain. *Brain* **138**, 1738-1755 (2015).
8. Stancu, I.C., *et al.* Aggregated Tau activates NLRP3-ASC inflammasome exacerbating exogenously seeded and non-exogenously seeded Tau pathology in vivo. *Acta Neuropathol* **137**, 599-617 (2019).
9. Ising, C., *et al.* NLRP3 inflammasome activation drives tau pathology. *Nature* **575**, 669-673 (2019).
10. Rexach, J.E., *et al.* Tau Pathology Drives Dementia Risk-Associated Gene Networks toward Chronic Inflammatory States and Immunosuppression. *Cell Rep* **33**, 108398 (2020).
11. Allen, M., *et al.* Divergent brain gene expression patterns associate with distinct cell-specific tau neuropathology traits in progressive supranuclear palsy. *Acta Neuropathol* **136**, 709-727 (2018).
12. Wang, H., *et al.* Genome-wide RNAseq study of the molecular mechanisms underlying microglia activation in response to pathological tau perturbation in the rTg4510 tau transgenic animal model. *Mol Neurodegener* **13**, 65 (2018).

13. Friedman, B.A., *et al.* Diverse Brain Myeloid Expression Profiles Reveal Distinct Microglial Activation States and Aspects of Alzheimer's Disease Not Evident in Mouse Models. *Cell Rep* **22**, 832-847 (2018).
14. Matarin, M., *et al.* A genome-wide gene-expression analysis and database in transgenic mice during development of amyloid or tau pathology. *Cell Rep* **10**, 633-644 (2015).
15. Stanley, E.R. & Chitu, V. CSF-1 receptor signaling in myeloid cells. *Cold Spring Harb Perspect Biol* **6**(2014).
16. Cannarile, M.A., *et al.* Colony-stimulating factor 1 receptor (CSF1R) inhibitors in cancer therapy. *J Immunother Cancer* **5**, 53 (2017).
17. Asai, H., *et al.* Depletion of microglia and inhibition of exosome synthesis halt tau propagation. *Nat Neurosci* **18**, 1584-1593 (2015).
18. Shi, Y., *et al.* Microglia drive APOE-dependent neurodegeneration in a tauopathy mouse model. *J Exp Med* **216**, 2546-2561 (2019).
19. Mancuso, R., *et al.* CSF1R inhibitor JNJ-40346527 attenuates microglial proliferation and neurodegeneration in P301S mice. *Brain* **142**, 3243-3264 (2019).
20. Bennett, R.E., *et al.* Partial reduction of microglia does not affect tau pathology in aged mice. *J Neuroinflammation* **15**, 311 (2018).
21. Condello, C., DeGrado, W.F. & Prusiner, S.B. Prion biology: implications for Alzheimer's disease therapeutics. *Lancet Neurol* **19**, 802-803 (2020).
22. Allen, B., *et al.* Abundant tau filaments and nonapoptotic neurodegeneration in transgenic mice expressing human P301S tau protein. *J Neurosci* **22**, 9340-9351 (2002).
23. Goedert, M., Jakes, R. & Crowther, R.A. Effects of frontotemporal dementia FTDP-17 mutations on heparin-induced assembly of tau filaments. *FEBS Lett* **450**, 306-311 (1999).
24. Sperfeld, A.D., *et al.* FTDP-17: an early-onset phenotype with parkinsonism and epileptic seizures caused by a novel mutation. *Ann Neurol* **46**, 708-715 (1999).
25. Johnson, N.R., *et al.* Evidence for sortilin modulating regional accumulation of human tau prions in transgenic mice. *Proc Natl Acad Sci U S A* **114**, E11029-E11036 (2017).
26. Tap, W.D., *et al.* Structure-Guided Blockade of CSF1R Kinase in Tenosynovial Giant-Cell Tumor. *N Engl J Med* **373**, 428-437 (2015).
27. Spangenberg, E., *et al.* Sustained microglial depletion with CSF1R inhibitor impairs parenchymal plaque development in an Alzheimer's disease model. *Nat Commun* **10**, 3758 (2019).
28. Sanders, D.W., *et al.* Distinct tau prion strains propagate in cells and mice and define different tauopathies. *Neuron* **82**, 1271-1288 (2014).
29. Aoyagi, A., *et al.* Abeta and tau prion-like activities decline with longevity in the Alzheimer's disease human brain. *Sci Transl Med* **11**(2019).
30. Iba, M., *et al.* Synthetic tau fibrils mediate transmission of neurofibrillary tangles in a transgenic mouse model of Alzheimer's-like tauopathy. *J Neurosci* **33**, 1024-1037 (2013).
31. Kaufman, S.K., *et al.* Tau Prion Strains Dictate Patterns of Cell Pathology, Progression Rate, and Regional Vulnerability In Vivo. *Neuron* **92**, 796-812 (2016).
32. Seeley, W.W., Crawford, R.K., Zhou, J., Miller, B.L. & Greicius, M.D. Neurodegenerative diseases target large-scale human brain networks. *Neuron* **62**, 42-52 (2009).
33. Gustke, N., Trinczek, B., Biernat, J., Mandelkow, E.M. & Mandelkow, E. Domains of tau protein and interactions with microtubules. *Biochemistry* **33**, 9511-9522 (1994).
34. Lei, F., *et al.* CSF1R inhibition by a small-molecule inhibitor is not microglia specific; affecting hematopoiesis and the function of macrophages. *Proc Natl Acad Sci U S A* **117**, 23336-23338 (2020).
35. Bellver-Landete, V., *et al.* Microglia are an essential component of the neuroprotective scar that forms after spinal cord injury. *Nat Commun* **10**, 518 (2019).
36. Luo, J., *et al.* Colony-stimulating factor 1 receptor (CSF1R) signaling in injured neurons facilitates protection and survival. *J Exp Med* **210**, 157-172 (2013).

37. Jul, P., *et al.* Hyperactivity with Agitative-Like Behavior in a Mouse Tauopathy Model. *Journal of Alzheimer's disease : JAD* **49**, 783-795 (2016).
38. Dumont, M., *et al.* Behavioral deficit, oxidative stress, and mitochondrial dysfunction precede tau pathology in P301S transgenic mice. *FASEB J* **25**, 4063-4072 (2011).
39. Wang, X., *et al.* Early intervention of tau pathology prevents behavioral changes in the rTg4510 mouse model of tauopathy. *PLoS One* **13**, e0195486 (2018).
40. Bacioglu, M., *et al.* Neurofilament Light Chain in Blood and CSF as Marker of Disease Progression in Mouse Models and in Neurodegenerative Diseases. *Neuron* **91**, 56-66 (2016).
41. Ashton, N.J., *et al.* Increased plasma neurofilament light chain concentration correlates with severity of post-mortem neurofibrillary tangle pathology and neurodegeneration. *Acta Neuropathol Commun* **7**, 5 (2019).
42. Rojas, J.C., *et al.* CSF neurofilament light chain and phosphorylated tau 181 predict disease progression in PSP. *Neurology* **90**, e273-e281 (2018).
43. Benner, B., *et al.* Pexidartinib, a Novel Small Molecule CSF-1R Inhibitor in Use for Tenosynovial Giant Cell Tumor: A Systematic Review of Pre-Clinical and Clinical Development. *Drug Des Devel Ther* **14**, 1693-1704 (2020).
44. Ke, Y.D., *et al.* CNS cell type-specific gene profiling of P301S tau transgenic mice identifies genes dysregulated by progressive tau accumulation. *J Biol Chem* **294**, 14149-14162 (2019).
45. Wu, Y.E., Pan, L., Zuo, Y., Li, X. & Hong, W. Detecting Activated Cell Populations Using Single-Cell RNA-Seq. *Neuron* **96**, 313-329 e316 (2017).
46. Tullai, J.W., *et al.* Immediate-early and delayed primary response genes are distinct in function and genomic architecture. *J Biol Chem* **282**, 23981-23995 (2007).
47. Watts, J.C., *et al.* Bioluminescence imaging of Abeta deposition in bigenic mouse models of Alzheimer's disease. *Proc Natl Acad Sci U S A* **108**, 2528-2533 (2011).
48. Tamguney, G., *et al.* Measuring prions by bioluminescence imaging. *Proc Natl Acad Sci U S A* **106**, 15002-15006 (2009).
49. Bellucci, A., *et al.* Induction of inflammatory mediators and microglial activation in mice transgenic for mutant human P301S tau protein. *The American journal of pathology* **165**, 1643-1652 (2004).
50. Ishizawa, K. & Dickson, D.W. Microglial activation parallels system degeneration in progressive supranuclear palsy and corticobasal degeneration. *J Neuropathol Exp Neurol* **60**, 647-657 (2001).
51. Gerhard, A., *et al.* In vivo imaging of microglial activation with [11C](R)-PK11195 PET in progressive supranuclear palsy. *Mov Disord* **21**, 89-93 (2006).
52. Keren-Shaul, H., *et al.* A Unique Microglia Type Associated with Restricting Development of Alzheimer's Disease. *Cell* **169**, 1276-1290 e1217 (2017).
53. Mucha, P.J., Richardson, T., Macon, K., Porter, M.A. & Onnela, J.P. Community structure in time-dependent, multiscale, and multiplex networks. *Science* **328**, 876-878 (2010).
54. Neuner, S.M., Heuer, S.E., Huentelman, M.J., O'Connell, K.M.S. & Kaczorowski, C.C. Harnessing Genetic Complexity to Enhance Translatability of Alzheimer's Disease Mouse Models: A Path toward Precision Medicine. *Neuron* **101**, 399-411 e395 (2019).
55. Liu, Y., *et al.* Concentration-dependent effects of CSF1R inhibitors on oligodendrocyte progenitor cells ex vivo and in vivo. *Exp Neurol* **318**, 32-41 (2019).
56. Dagher, N.N., *et al.* Colony-stimulating factor 1 receptor inhibition prevents microglial plaque association and improves cognition in 3xTg-AD mice. *J Neuroinflammation* **12**, 139 (2015).
57. Spangenberg, E.E., *et al.* Eliminating microglia in Alzheimer's mice prevents neuronal loss without modulating amyloid-beta pathology. *Brain* **139**, 1265-1281 (2016).

58. Gamache, J., *et al.* Factors other than hTau overexpression that contribute to tauopathy-like phenotype in rTg4510 mice. *Nat Commun* **10**, 2479 (2019).
59. Krasemann, S., *et al.* The TREM2-APOE Pathway Drives the Transcriptional Phenotype of Dysfunctional Microglia in Neurodegenerative Diseases. *Immunity* **47**, 566-581 e569 (2017).
60. Kang, S.S., *et al.* Microglial translational profiling reveals a convergent APOE pathway from aging, amyloid, and tau. *J Exp Med* **215**, 2235-2245 (2018).
61. Dejanovic, B., *et al.* Changes in the Synaptic Proteome in Tauopathy and Rescue of Tau-Induced Synapse Loss by C1q Antibodies. *Neuron* **100**, 1322-1336 e1327 (2018).
62. Litvinchuk, A., *et al.* Complement C3aR Inactivation Attenuates Tau Pathology and Reverses an Immune Network Deregulated in Tauopathy Models and Alzheimer's Disease. *Neuron* **100**, 1337-1353 e1335 (2018).
63. Wu, T., *et al.* Complement C3 Is Activated in Human AD Brain and Is Required for Neurodegeneration in Mouse Models of Amyloidosis and Tauopathy. *Cell Rep* **28**, 2111-2123 e2116 (2019).
64. Liddelow, S.A., *et al.* Neurotoxic reactive astrocytes are induced by activated microglia. *Nature* **541**, 481-487 (2017).
65. Yun, S.P., *et al.* Block of A1 astrocyte conversion by microglia is neuroprotective in models of Parkinson's disease. *Nat Med* **24**, 931-938 (2018).
66. Kodama, L., *et al.* Microglial microRNAs mediate sex-specific responses to tau pathology. *Nat Neurosci* **23**, 167-171 (2020).
67. Guneykaya, D., *et al.* Transcriptional and Translational Differences of Microglia from Male and Female Brains. *Cell Rep* **24**, 2773-2783 e2776 (2018).
68. Berve, K., West, B.L., Martini, R. & Groh, J. Sex- and region-biased depletion of microglia/macrophages attenuates CLN1 disease in mice. *J Neuroinflammation* **17**, 323 (2020).
69. Busche, M.A., *et al.* Tau impairs neural circuits, dominating amyloid-beta effects, in Alzheimer models in vivo. *Nat Neurosci* **22**, 57-64 (2019).
70. Vinet, J., *et al.* Neuroprotective function for ramified microglia in hippocampal excitotoxicity. *J Neuroinflammation* **9**, 27 (2012).
71. Badimon, A., *et al.* Negative feedback control of neuronal activity by microglia. *Nature* **586**, 417-423 (2020).
72. Liu, M., *et al.* Microglia depletion exacerbates acute seizures and hippocampal neuronal degeneration in mouse models of epilepsy. *Am J Physiol Cell Physiol* **319**, C605-C610 (2020).
73. Sosna, J., *et al.* Early long-term administration of the CSF1R inhibitor PLX3397 ablates microglia and reduces accumulation of intraneuronal amyloid, neuritic plaque deposition and pre-fibrillar oligomers in 5XFAD mouse model of Alzheimer's disease. *Mol Neurodegener* **13**, 11 (2018).
74. Son, Y., *et al.* Inhibition of Colony-Stimulating Factor 1 Receptor by PLX3397 Prevents Amyloid Beta Pathology and Rescues Dopaminergic Signaling in Aging 5xFAD Mice. *Int J Mol Sci* **21**(2020).
75. Pinto, B., *et al.* Rescuing Over-activated Microglia Restores Cognitive Performance in Juvenile Animals of the Dp(16) Mouse Model of Down Syndrome. *Neuron* **108**, 887-904 e812 (2020).
76. Goedert, M., Clavaguera, F. & Tolnay, M. The propagation of prion-like protein inclusions in neurodegenerative diseases. *Trends Neurosci* **33**, 317-325 (2010).
77. Hanseeuw, B.J., *et al.* Association of Amyloid and Tau With Cognition in Preclinical Alzheimer Disease: A Longitudinal Study. *JAMA Neurol* (2019).
78. Hillmer, A.T., *et al.* Microglial depletion and activation: A [(11)C]PBR28 PET study in nonhuman primates. *EJNMMI Res* **7**, 59 (2017).

79. Butowski, N., *et al.* Orally administered colony stimulating factor 1 receptor inhibitor PLX3397 in recurrent glioblastoma: an Ivy Foundation Early Phase Clinical Trials Consortium phase II study. *Neuro Oncol* **18**, 557-564 (2016).
80. Reu, P., *et al.* The Lifespan and Turnover of Microglia in the Human Brain. *Cell Rep* **20**, 779-784 (2017).
81. Horti, A.G., *et al.* PET imaging of microglia by targeting macrophage colony-stimulating factor 1 receptor (CSF1R). *Proc Natl Acad Sci U S A* **116**, 1686-1691 (2019).
82. Gibbons, G.S., *et al.* Conformation-selective tau monoclonal antibodies inhibit tau pathology in primary neurons and a mouse model of Alzheimer's disease. *Mol Neurodegener* **15**, 64 (2020).
83. Yanamandra, K., *et al.* Anti-tau antibody reduces insoluble tau and decreases brain atrophy. *Ann Clin Transl Neurol* **2**, 278-288 (2015).
84. Lee, S.H., *et al.* Antibody-Mediated Targeting of Tau In Vivo Does Not Require Effector Function and Microglial Engagement. *Cell Rep* **16**, 1690-1700 (2016).
85. Elmore, M.R., *et al.* Colony-stimulating factor 1 receptor signaling is necessary for microglia viability, unmasking a microglia progenitor cell in the adult brain. *Neuron* **82**, 380-397 (2014).
86. Duong, H. & Han, M. A multispectral LED array for the reduction of background autofluorescence in brain tissue. *J Neurosci Methods* **220**, 46-54 (2013).
87. Kfoury, N., Holmes, B.B., Jiang, H., Holtzman, D.M. & Diamond, M.I. Trans-cellular propagation of Tau aggregation by fibrillar species. *J Biol Chem* **287**, 19440-19451 (2012).
88. Barghorn, S., Biernat, J. & Mandelkow, E. Purification of recombinant tau protein and preparation of Alzheimer-paired helical filaments in vitro. *Methods Mol Biol* **299**, 35-51 (2005).
89. Zhang, Y., *et al.* Purification and Characterization of Progenitor and Mature Human Astrocytes Reveals Transcriptional and Functional Differences with Mouse. *Neuron* **89**, 37-53 (2016).
90. Schmittgen, T.D. & Livak, K.J. Analyzing real-time PCR data by the comparative C(T) method. *Nat Protoc* **3**, 1101-1108 (2008).

FIGURES

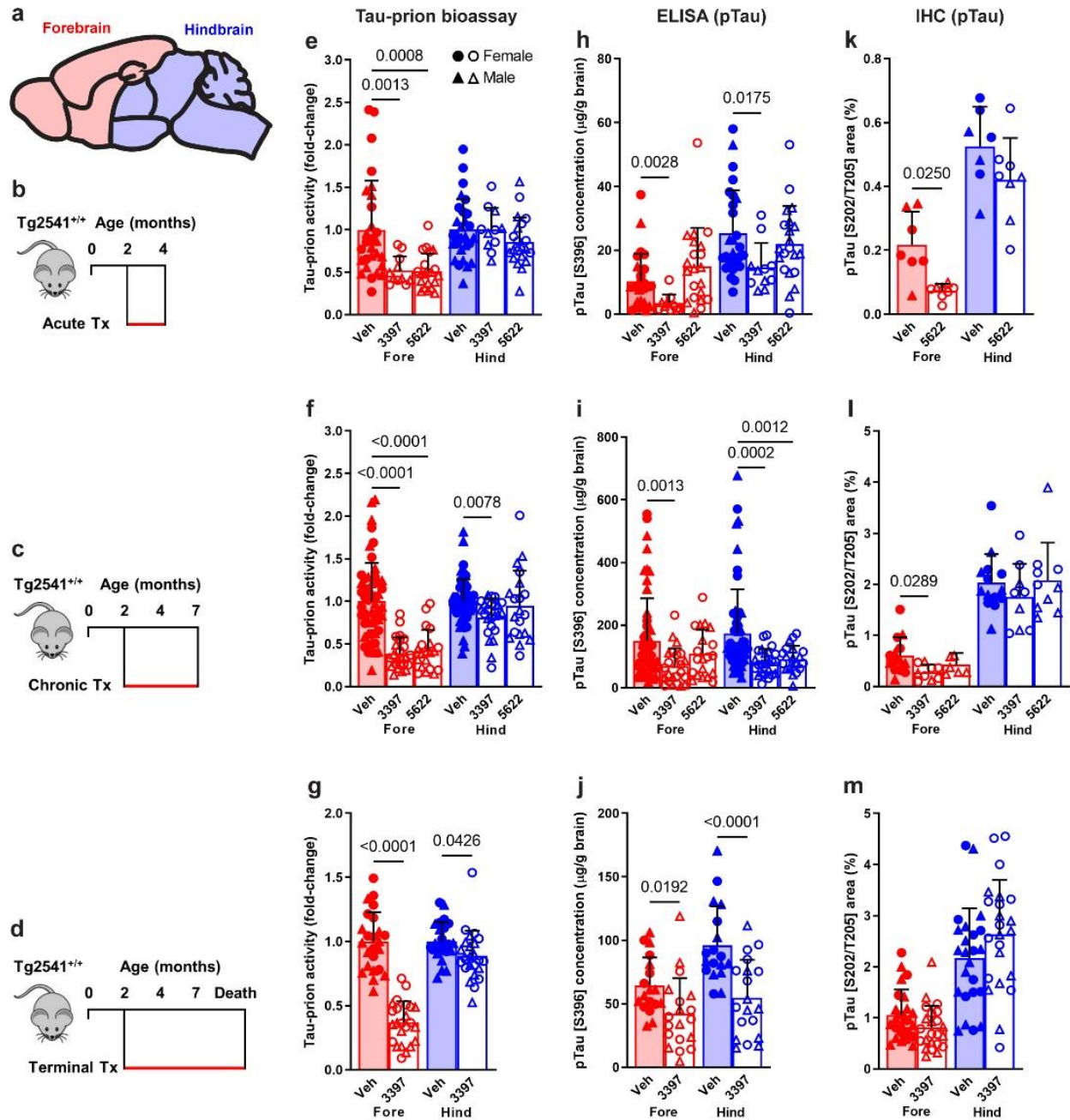


Fig. 1| CSF1R inhibition by three treatment paradigms reduces pathogenic tau levels in the brains of Tg2541 mice. **a**, Sagittal view of the mouse brain divided into two regions: the forebrain, containing the cortex, hippocampus, striatum, and olfactory bulb; and the hindbrain, containing the thalamus, hypothalamus, midbrain, cerebellum, and brain stem. **b-d**, Schematics of acute (**b**), chronic (**c**), or terminal (**d**) PLX treatment of Tg2541 mice from 2–4 mo of age, 2–7

mo of age, or 2 mo of age until death, respectively. **e–g**, Tau-prion levels in forebrain and hindbrain tissue homogenates of Tg2541 mice receiving acute (**e**), chronic (**f**), or terminal (**g**) treatment with vehicle, PLX3397 (275 mg/kg oral), or PLX5622 (1200 mg/kg oral), measured using the HEK293T cell tau-prion bioassay and normalized to the vehicle-treated group. **h–j**, Levels of pTau [S396] measured by ELISA in formic acid extracts of forebrain and hindbrain tissue homogenates of Tg2541 mice receiving acute (**h**), chronic (**i**), or terminal treatment (**j**) with vehicle, PLX3397, or PLX5622, normalized to total protein concentration. **k–m**, Quantification of pTau [S202/T205]-positive area by IHC analysis of forebrain and hindbrain areas of Tg2541 mice receiving acute (**k**), chronic (**l**), or terminal (**m**) treatment with vehicle, PLX3397, or PLX5622. In **e–m**, each symbol represents the forebrain or hindbrain of an individual mouse, with female mice shown as closed or open circles and male mice shown as closed or open triangles. Error bars represent the s.d. of the mean. Welch ANOVA with Dunnett T3 post hoc testing was used in **e**, **f**, **h**, **i**, and **l**. Two-way ANOVA with Holm-Šidák post hoc testing was used in **g**, **j**, **k**, and **m**. *P* values for all statistically significant differences ($P < 0.05$) are shown.

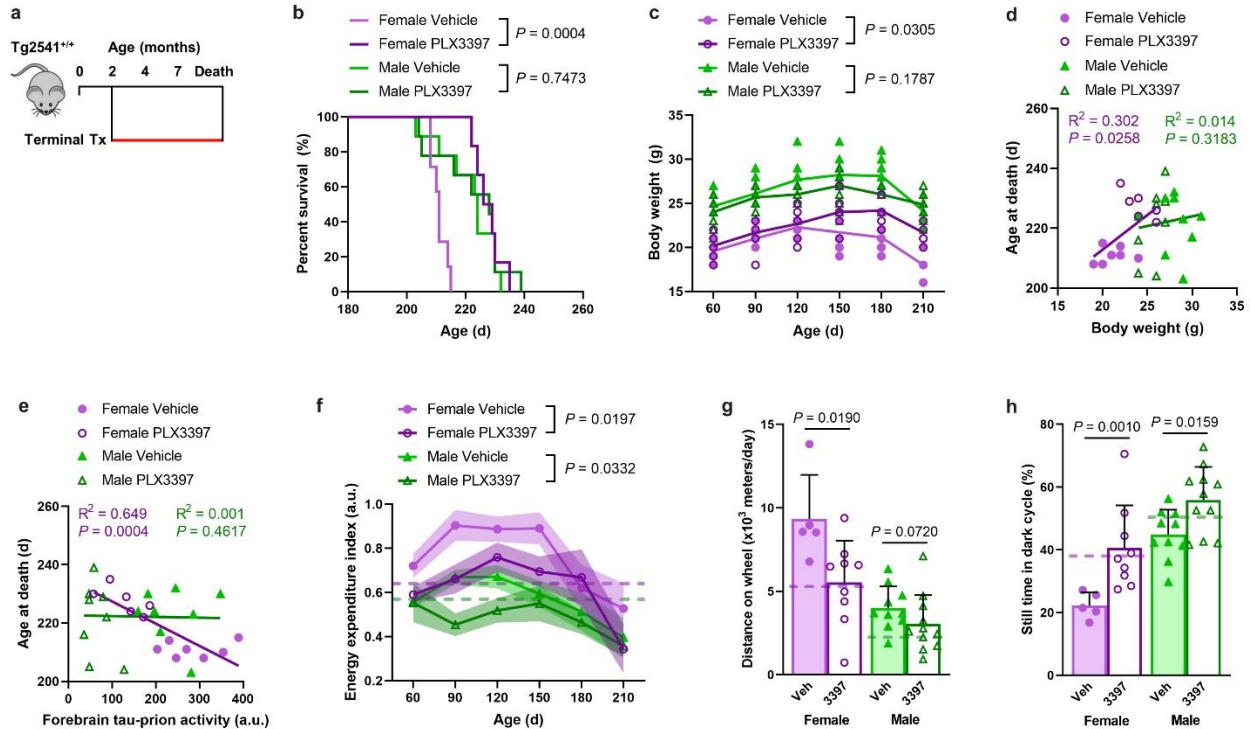


Fig. 2| CSF1R inhibition extends survival of female Tg2541 mice. **a**, Schematic of terminal PLX3397 treatment (275 mg/kg oral) of Tg2541 mice from 2 mo of age until death. **b**, Kaplan-Meier plot showing percent survival of female or male Tg2541 mice treated with vehicle or PLX3397. $n=7$ mice for Female Vehicle; $n=6$ mice for Female PLX3397; $n=9$ mice for Male Vehicle; $n=9$ mice for Male PLX3397. Differences in survival between vehicle and PLX3397 treatment in female or male mice were evaluated by Log-rank (Mantel-Cox) test. **c**, Body weights of female or male Tg2541 mice treated with vehicle or PLX3397. Each symbol represents an individual mouse and lines indicate group means. Differences in weight between vehicle and PLX3397 treatment in female or male mice were evaluated by mixed-effects analysis (Restricted maximum likelihood). **d,e**, Correlation plots for body weight at 180 d of age (**d**) or forebrain tau-prion activity at death (**e**) and survival for female or male Tg2541 mice treated with vehicle or PLX3397. Each symbol represents an individual mouse and linear regression lines are shown for female or male mice, with vehicle- and PLX3397-treated mice combined. Pearson's correlation analysis was performed and the results are shown. **f**, Longitudinal energy expenditure indices (see Methods) of female or male Tg2541 mice treated with vehicle or PLX3397. Symbols represent the group means and shaded regions indicate the s.d. of the mean. Group sizes are the same as shown in **g** and **h**. Differences between vehicle and PLX3397 treatment in female or male mice were assessed by three-way repeated

measures ANOVA. **g,h**, Average distance traveled on the running wheel (**g**) or still time during the dark cycle (**h**) in female or male Tg2541 mice treated with vehicle or PLX3397, and measured between 90-d-old and 150-d-old. Differences between vehicle and PLX3397 treatment in female or male mice were assessed by Mann-Whitney test. In **c–h**, female mice are shown as closed or open circles and male mice are shown as closed or open triangles. In **f–h**, the dashed lines indicate the same measurements in 90-d-old wildtype mice.

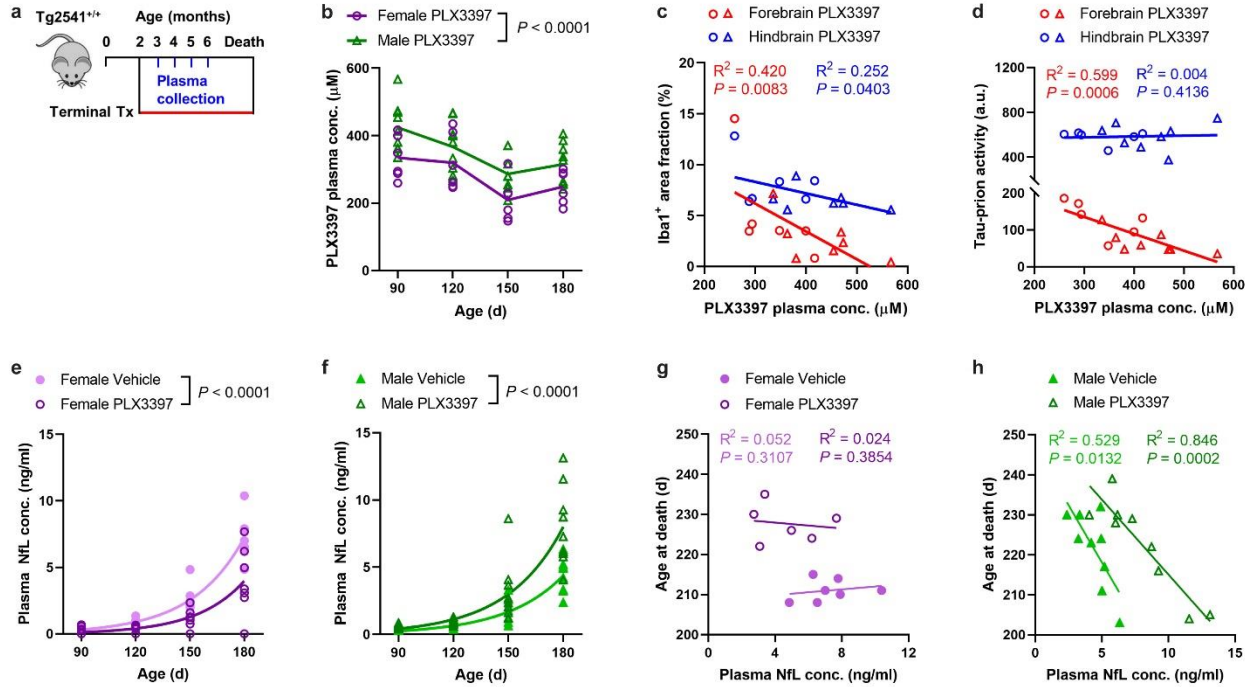


Fig. 3| Plasma levels of PLX3397 and NfL correlate with tauopathy disease course. a, Schematic of terminal PLX3397 treatment (275 mg/kg oral) of Tg2541 mice from 2 mo of age until death and blood plasma collected at 3, 4, 5, and 6 mo of age. **b,** Plasma concentration of PLX3397 in female or male Tg2541 mice. The difference between female and male mice was assessed by two-way repeated measures ANOVA. **c,d,** Correlation plots for plasma concentration of PLX3397 at 90 d age and Iba1 area fraction by IHC (**c**) or tau-prion activity (**d**) in the forebrains or hindbrains of Tg2541 mice at death. Female mice are shown as open circles and male mice shown as open triangles. Linear regression was performed with female and male mice combined and best-fit lines are shown. Pearson's correlation analysis was performed and the results are shown. **e,f,** Plasma concentration of NfL in female (**e**) or male (**f**) Tg2541 mice treated with vehicle or PLX3397. The differences between vehicle or PLX3397 treatment were evaluated by non-linear regression using exponential growth models and the best-fit lines and statistical results are shown. **g,h,** Correlation plots for plasma NfL concentration and survival in female (**g**) or male (**h**) Tg2541 mice. Linear regression and Pearson's correlation analysis were performed and the results are shown.

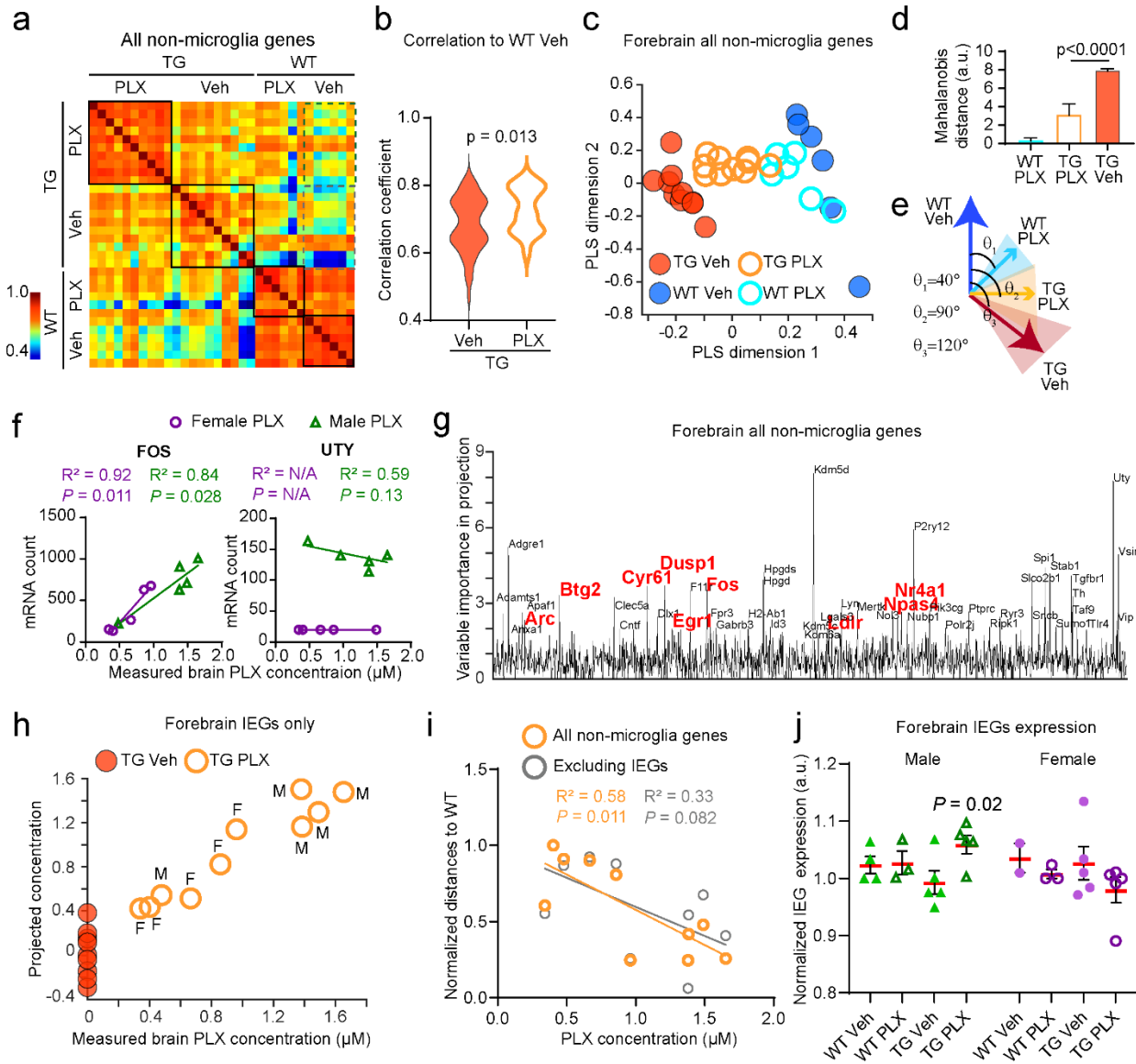


Fig. 4| PLX treatment normalizes gene expression profile, but dose-dependent excitotoxicity occurs with higher drug exposure. **a**, Pearson's correlations among individual mice for non-microglia gene expression patterns (1,599 genes for each mouse). Mice from the same treatment group (black boxes) show a high degree of correlations. Dashed boxes show correlations of Tg2541 mice and wildtype vehicle group mice. **b**, Distributions of correlation coefficients in the two groups in dashed boxes in **a**. **c**, Partial least square (PLS) regression scores and projections of non-microglia gene expression patterns in different groups (1,599 genes for each mouse). The first two dimensions are shown covering >95% of the total variance. Vehicle-treated mice (filled dots) were used for regression (five dimensions covering

99.99% of the total variance) and PLX5622-treated (1200 mg/kg oral) mice (circles) were projected onto the regression dimensions. **d**, Mahalanobis population vector distances of gene expression patterns in PLS dimensions relative to the wildtype vehicle group. Mann-Whitney test was used for statistical comparison. **e**, Population vector angles of gene expression patterns in PLS dimensions from different treatment groups. **f**, Example plots of measured brain PLX concentration against mRNA counts for a PLX-modulated gene (*FOS*) and a sex-modulated gene (*UTY*). Linear regression and Pearson's correlation analysis were performed and the results are shown. **g**, Variable importance in projection (VIP) scores in a PLS regression using non-microglial gene expression patterns to brain PLX concentration and sex. Genes with VIP scores above 2 are labeled. Red fonts indicate a subset that belongs to immediate early genes (IEGs). **h**, Scatter plot of measured vs. projected brain PLX concentration, which was based on a PLS regression with IEG expression. **i**, Correlation of brain PLX concentration and the population vector distances between PLX-treated individual mouse transcriptome pattern to WT, with and without the IEGs (1,599 and 1,543 genes for each mouse, respectively). Linear regressions were calculated for each group. **j**, Quantification of normalized expression levels from all IEGs (56 genes for each mouse) in forebrain. Each group is compared to 1 using one-sample t-test.

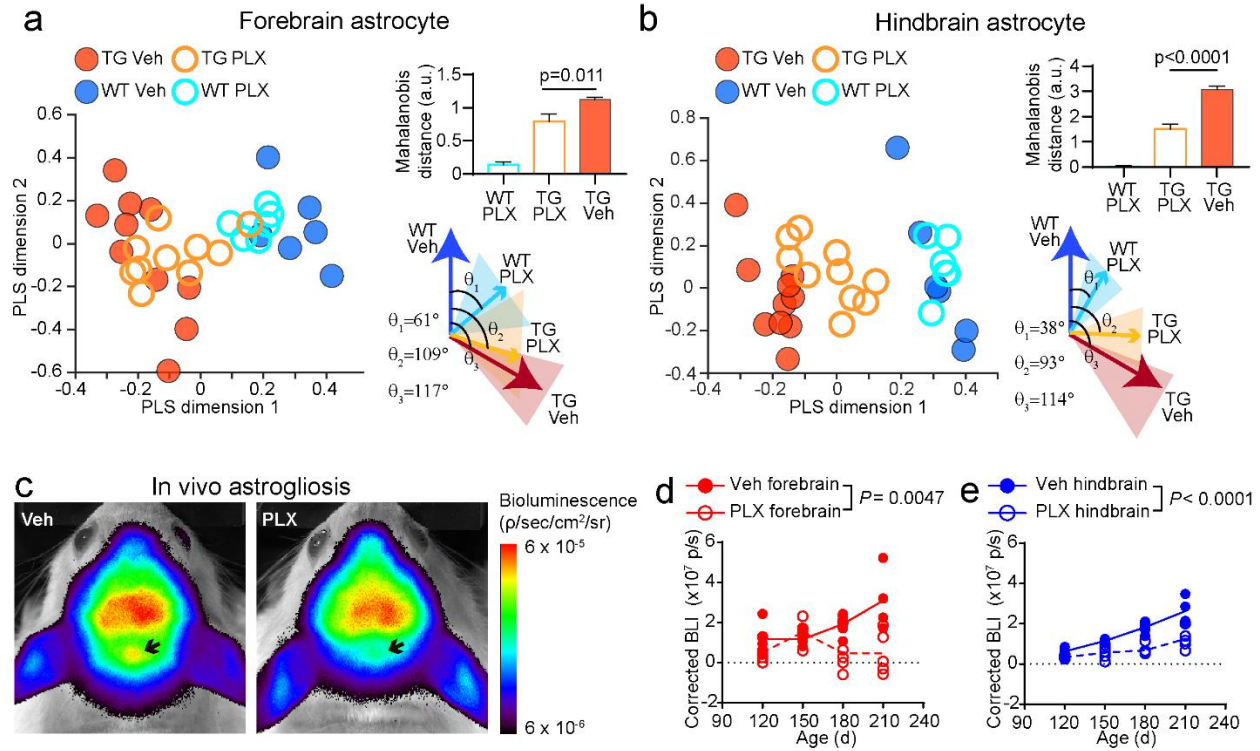


Fig. 5 | PLX-treatment ameliorates tau-induced pathological astrocyte activation. a, b, Analyses similar to Fig. 4c–e using astrocyte-specific genes (47 genes in each mouse) in (a) forebrain and (b) hindbrain regions. For other cell types and brain regions, see Supplementary Fig. 12. **c,** Representative images of *in vivo* bioluminescence imaging of GFAP activity in Tg2541 mice with vehicle or PLX3397 treatment. Arrows indicate hindbrain regions. **d, e,** Quantifications of longitudinal measurements of astroglia-driven bioluminescence in the (d) forebrains or (e) hindbrains of Tg2541 mice with vehicle or PLX3397 treatment. Differences in BLI signal between vehicle and PLX treatment were evaluated by mixed-effects analysis (Restricted maximum likelihood).

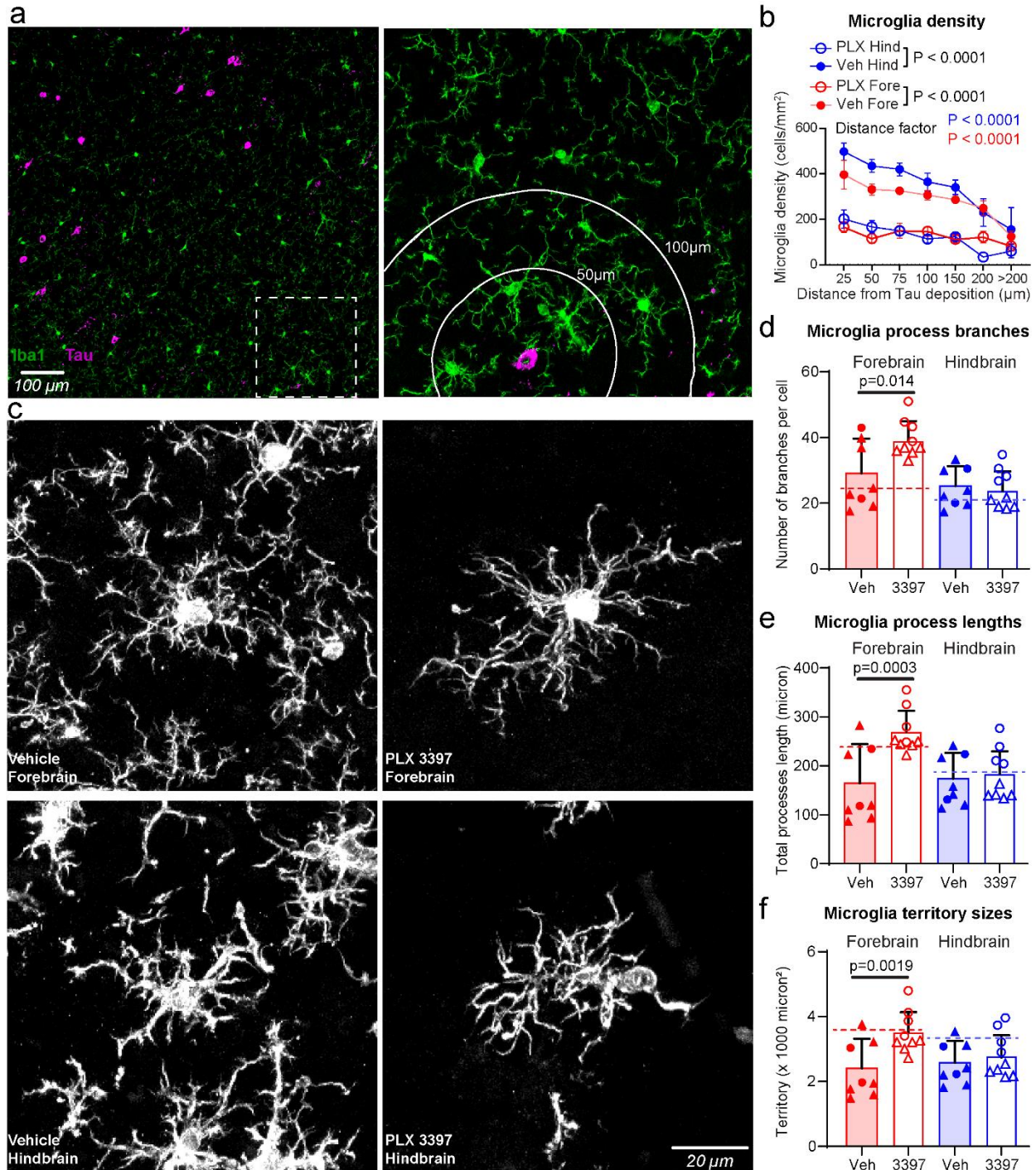


Fig. 6| PLX3397 treatment preferentially eliminates reactive microglia around tau deposits. **a**, Representative confocal images of immunostaining of tau protein (magenta) and microglia (Iba1, green) in the brain of a vehicle-treated 210-d-old Tg2541 mouse. The right panel shows the zoomed image from the dashed box in the left panel. The white lines in the right panel show distances from the tau deposit at the center. **b**, Quantification of microglial

densities at different distances from the nearest tau deposit in Tg2541 mice treated with vehicle or PLX3397 (275 mg/kg oral). Two-way ANOVA was used to compare statistical differences between treatment groups and distance bins. **c**, Representative confocal images of microglia processes labeled by Iba1 immunohistochemistry. **d–f**, Quantification of microglia processes branch numbers (**d**), total lengths (**e**) and territory sizes (**f**) in Tg2541 mice treated with vehicle or PLX3397. Each data point shows the average value of the microglia measured in an individual mouse. Error bars represent the s.d. of the mean. Circles indicate female mice and triangles indicate male mice. Dotted lines show the average measurements from microglia in wildtype mice. Mann-Whitney tests were used to compare between groups.

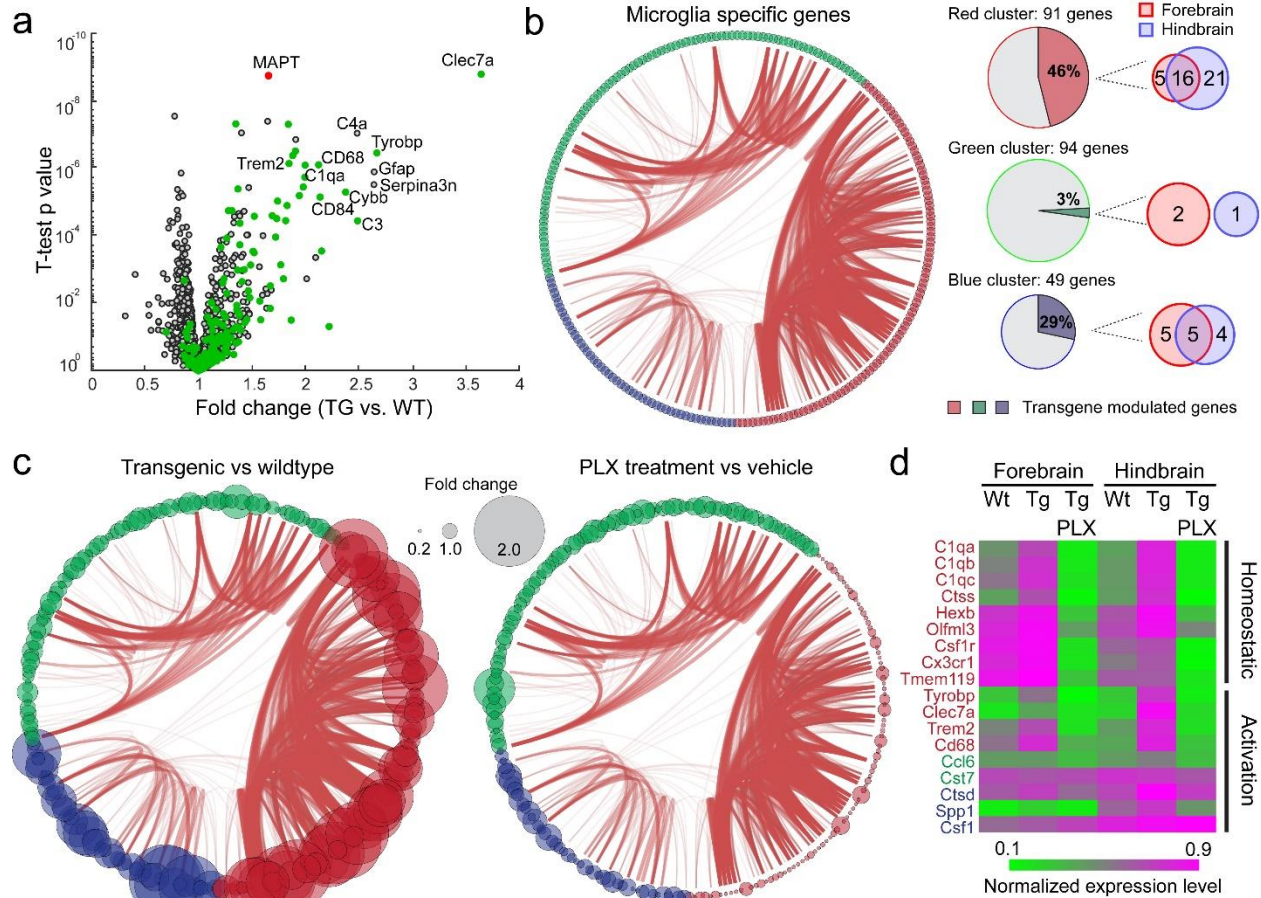
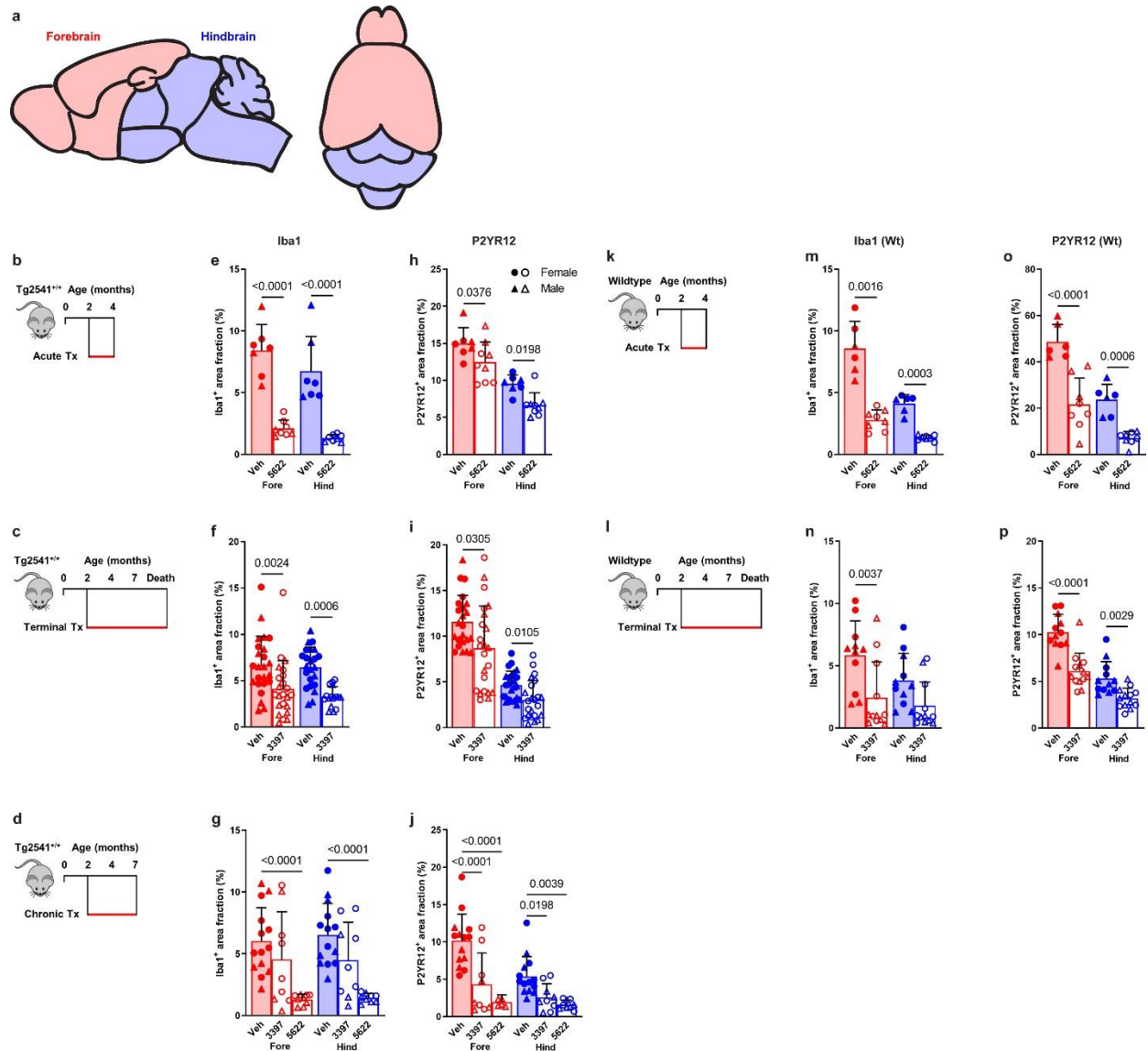


Fig. 7 | A transcriptome signature for tau-resistant and PLX5622-resistant microglia. a, Volcano plot of gene expression changes between Tg2541 and wildtype mice. Many microglial-specific genes (green dots) show trends of up-regulation in Tg2541 mice. **b,** Microglial-specific genes (242 genes in our dataset) are clustered into three groups: red, green and blue. Connecting arcs between genes represent the degree of correlation. The pie charts on the right show the percentage of genes in each group that are differentially expressed in Tg2541 and wildtype mice, and the Venn diagrams indicate the brain regions of differential expression. **c,** Schemaball graphs of microglial-specific genes comparing Tg2541 to wildtype, and Tg2541 vehicle to PLX5622 treatment (1200 mg/kg oral). Individual circle sizes indicate fold changes. **d,** Heatmap showing expression level changes in DAM genes⁵². Gene names are color coded to show their group assignments.

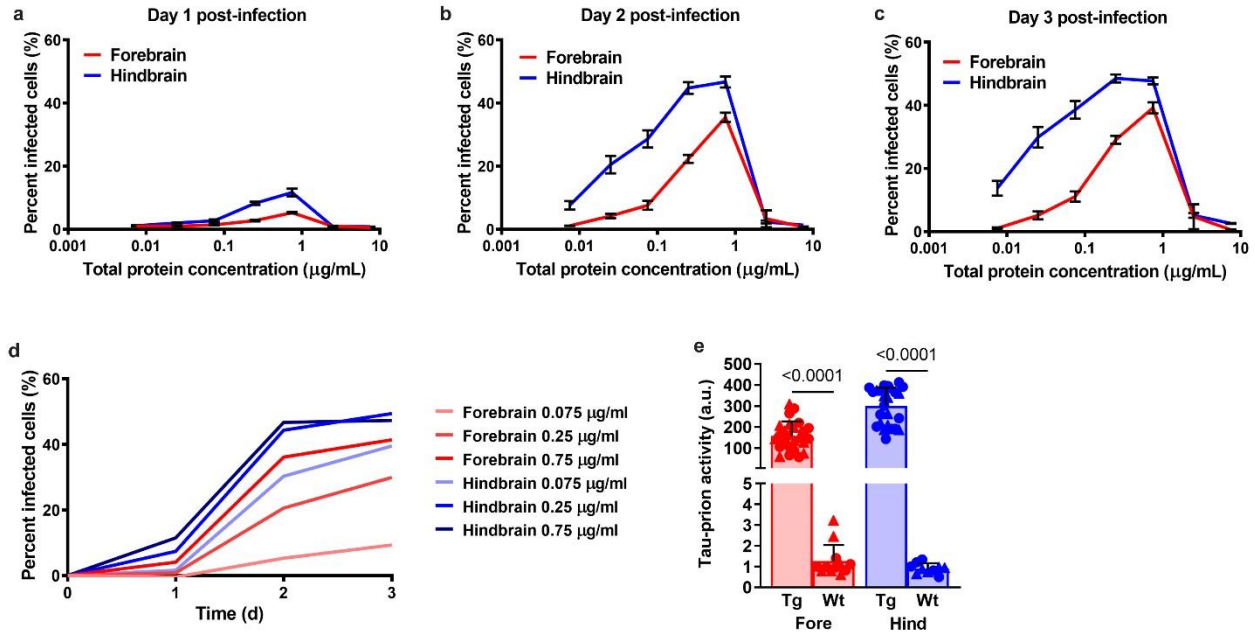
SUPPLEMENTARY INFORMATION



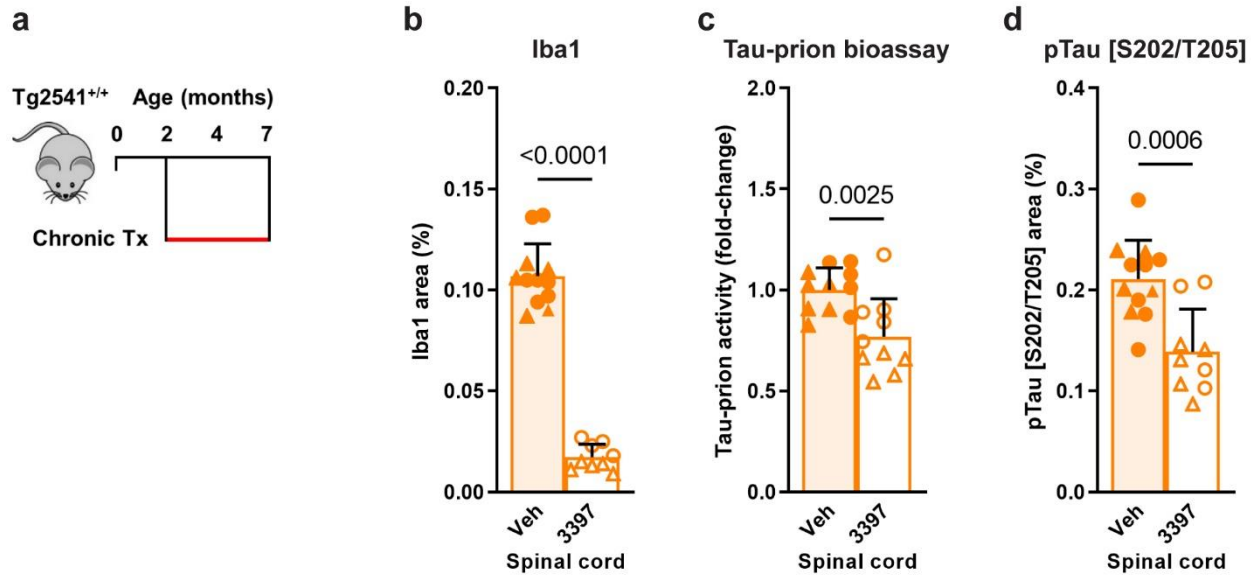
Supplementary Fig. 1| Microglial depletion by CSF1R inhibitors in Tg2541 and wildtype mice.

a, Sagittal and superior diagrams of the mouse brain divided into two regions: the forebrain, containing the cortex, hippocampus, striatum, and olfactory bulb; and the hindbrain, containing the thalamus, hypothalamus, midbrain, cerebellum, and brain stem. **b–d**, Schematics of acute (**b**), terminal (**c**), or chronic (**d**) PLX treatment of Tg2541 mice from 2–4 mo of age, 2 mo of age until death, or 2–7 mo of age, respectively. **e–g**, Quantification of the Iba1-positive area fraction by IHC in the forebrains or hindbrains of Tg2541 mice receiving acute (**e**), terminal (**f**), or chronic (**g**) treatment with vehicle, PLX3397 (275 mg/kg oral), or PLX5622 (1200 mg/kg oral). **h–j**, Quantification of the P2YR12-positive area fraction by IHC in the forebrains or

hindbrains of Tg2541 mice receiving acute (**h**), terminal (**i**), or chronic (**j**) treatment with vehicle, PLX3397, or PLX5622. **k,l**, Schematics of acute (**k**) or terminal (**l**) PLX treatment of C57BL/6J wildtype mice (Wt) from 2-4 mo of age, or 2 mo of age until death, respectively. **m,n**, Quantification of the Iba1-positive area fraction by IHC in the forebrain and hindbrain of Wt mice receiving acute (**m**) or terminal (**n**) treatment with vehicle, PLX3397, or PLX5622. **o,p**, Quantification of the P2YR12-positive area fraction by IHC in the forebrains or hindbrains of Wt mice receiving acute (**o**) or terminal (**p**) treatment with vehicle, PLX3397, or PLX5622. In **e-j** and **m-p**, each symbol represents the forebrain or hindbrain of an individual mouse, with female mice shown as closed or open circles and male mice shown as closed or open triangles. Error bars represent s.d. of the mean. Two-way ANOVA with Holm-Šidák post hoc testing was used in **e, f, h, i**, and **m-p**. Welch ANOVA with Dunnett T3 post hoc testing was used for **g**. One-way ANOVA with Holm-Šidák post hoc testing was used for **j**. *P* values for all statistically significant differences ($P < 0.05$) are shown.

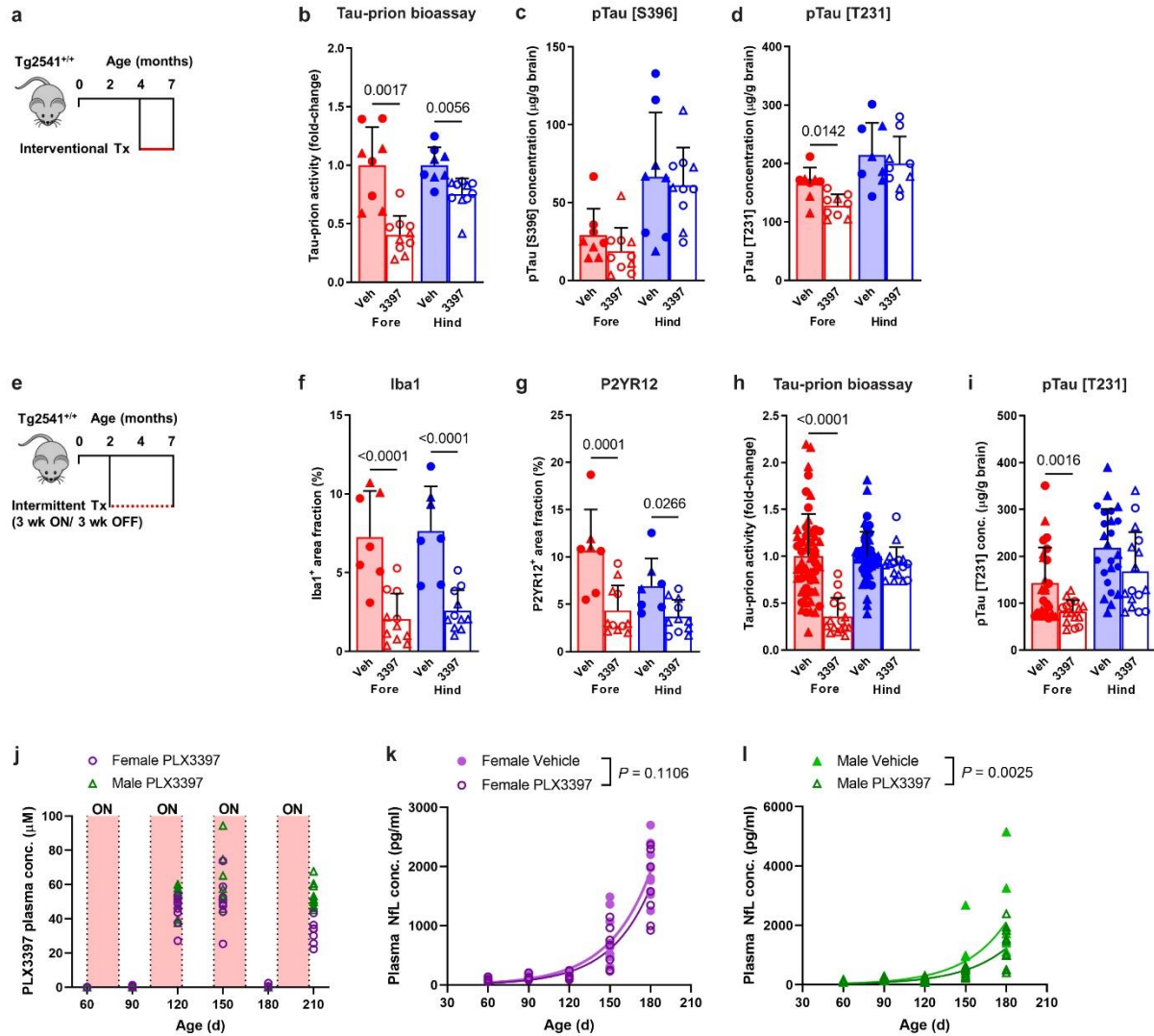


Supplementary Fig. 2| Optimization of HEK293T cell bioassay for measuring tau-prions in Tg2541 mouse brain homogenates. **a–c**, Percent of HEK293T cells expressing YFP-tau-RD*P301L/V337M with tau aggregates at one (**a**), two (**b**), or three (**c**) days post-infection with Tg2541 mouse forebrain or hindbrain homogenates at concentrations ranging from 0.0075–7.5 µg/ml. Error bars represent s.e.m. of three terminal Tg2541 mice. **d**, Percent of cells infected with tau aggregates over time following infection with 0.075, 0.25, or 0.75 µg/ml Tg2541 mouse forebrain or hindbrain homogenates. Lines represent the means of three terminal Tg2541 mice. **e**, Tau-prion levels in 0.25 µg/ml forebrain or hindbrain homogenates of Tg2541 (Tg) or Wildtype (Wt) mice, measured using the optimized HEK293T cell tau-prion bioassay. Each symbol represents the forebrain or hindbrain of an individual mouse and female mice are shown as closed circles while male mice are shown as closed triangles. Two-way ANOVA with Holm-Šidák post hoc testing was used and *P* values for all statistically significant differences (*P* < 0.05) are shown.



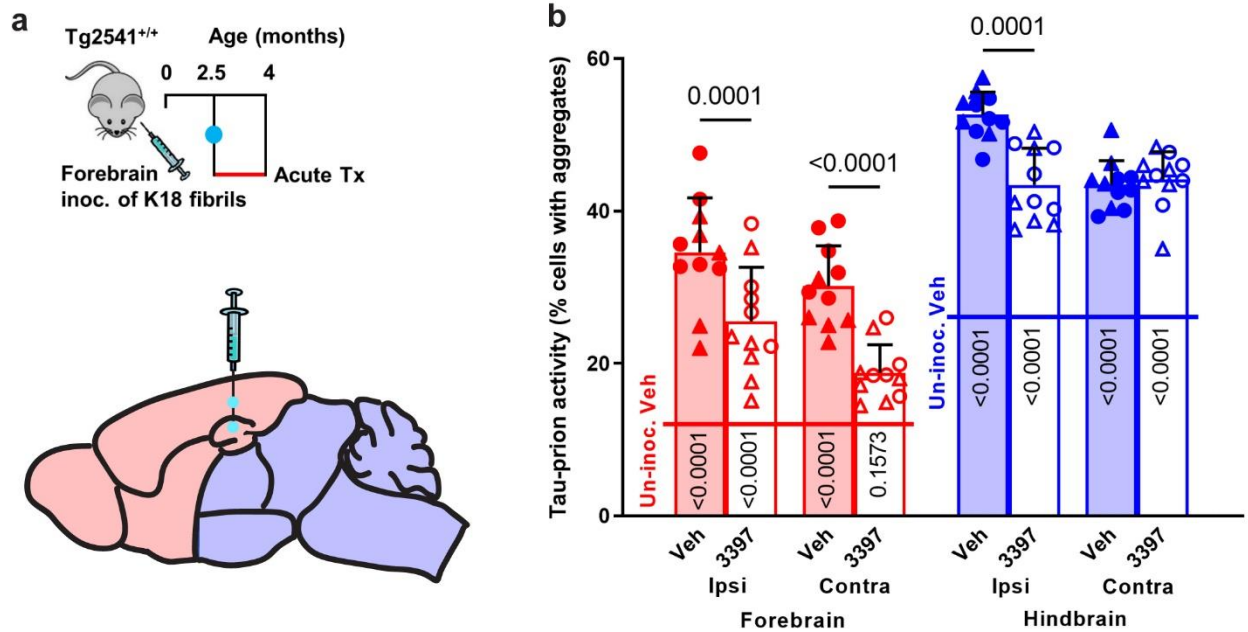
Supplementary Fig. 3| CSF1R inhibition reduces microglia and pathogenic tau levels in the spinal cords of Tg2541 mice.

a, Schematic of chronic PLX treatment of Tg2541 mice from 2–7 mo of age. **b**, Quantification of the Iba1-positive area fraction by IHC in the spinal cords of Tg2541 mice receiving chronic treatment with vehicle or PLX3397 (275 mg/kg oral). **c**, Tau-prion levels in spinal cord tissue homogenates of Tg2541 mice receiving chronic treatment with vehicle or PLX3397, measured using the HEK293T cell tau-prion bioassay and normalized to the vehicle group. **d**, Quantification of pTau [S202/T205]-positive area by IHC in the spinal cords of Tg2541 mice receiving chronic treatment with vehicle or PLX3397. In **b–d**, each symbol represents an individual mouse, with female mice shown as closed or open circles and male mice shown as closed or open triangles. Error bars represent s.d. of the mean. Unpaired t tests were used and *P* values for all statistically significant differences ($P < 0.05$) are shown.

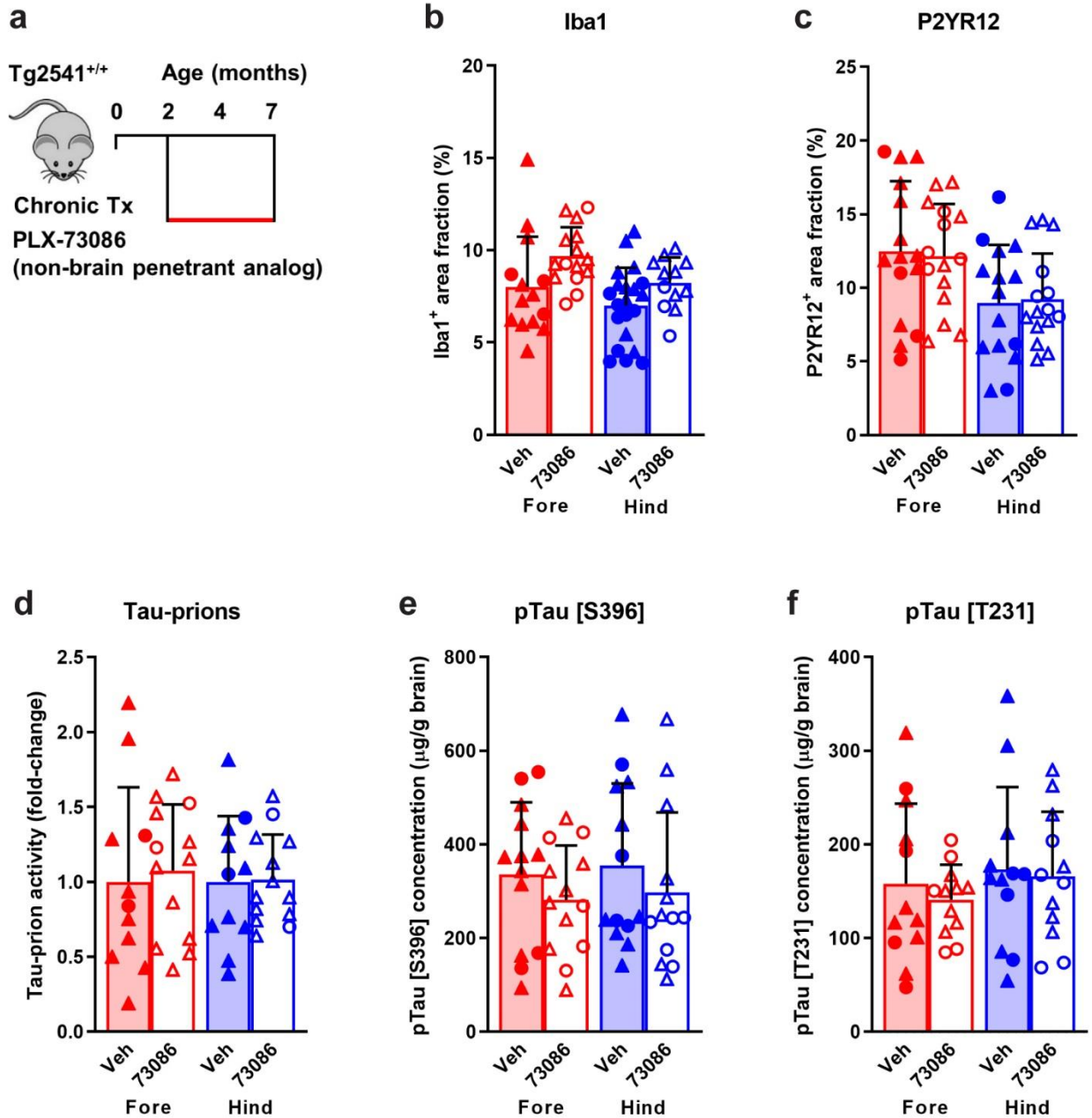


Supplementary Fig. 4| Interventional and intermittent CSF1R inhibition reduces pathogenic tau levels in the brains of Tg2541 mice. **a**, Schematic of interventional PLX treatment of Tg2541 mice from 4–7 mo of age. **b**, Tau-prion levels in forebrain and hindbrain tissue homogenates of Tg2541 mice receiving interventional treatment with vehicle or PLX3397 (275 mg/kg oral), measured using the HEK293T cell tau-prion bioassay and normalized to the vehicle group. **c**, Levels of pTau [S396] measured by ELISA in formic acid extracts of forebrain and hindbrain tissue homogenates of Tg2541 mice receiving interventional treatment with vehicle or PLX3397, normalized to total protein concentration. **d**, Levels of pTau [T231] measured by ELISA in formic acid extracts of forebrain and hindbrain tissue homogenates of Tg2541 mice receiving interventional treatment with vehicle or PLX3397, normalized to total protein concentration. **e**, Schematic of intermittent PLX treatment of Tg2541 mice from 2–7 mo of age, with three weeks on treatment followed by three weeks off of treatment. **f, g**,

Quantification of the Iba1-positive (**f**) or P2YR12-positive (**g**) area fractions by IHC in the forebrains or hindbrains of Tg2541 mice receiving intermittent treatment with vehicle or PLX3397. **h**, Tau-prion levels in forebrain and hindbrain tissue homogenates of Tg2541 mice receiving intermittent treatment with vehicle or PLX3397, measured using the HEK293T cell tau-prion bioassay and normalized to the vehicle group. **i**, Levels of pTau [T231] measured by ELISA in formic acid extracts of forebrain and hindbrain tissue homogenates of Tg2541 mice receiving intermittent treatment with vehicle or PLX3397, normalized to total protein concentration. **j**, Plasma concentration of PLX3397 in female or male Tg2541 mice receiving intermittent treatment, with shaded regions indicating periods that the mice were on PLX3397 treatment. Each symbol represents an individual mouse. Female mice are shown as open circles, male mice are shown as open triangles, and lines indicate the group means. **k,l**, Plasma concentration of NfL in female (**k**) or male (**l**) Tg2541 mice receiving intermittent treatment with vehicle or PLX3397. The differences between vehicle or PLX3397 treatment were evaluated by non-linear regression using exponential growth models and the best-fit lines and statistical results are shown. In **b-d** and **f-i**, each symbol represents the forebrain or hindbrain of an individual mouse, with female mice shown as closed or open circles and male mice shown as closed or open triangles. Error bars represent s.d. of the mean. Two-way ANOVA with Holm-Šidák post hoc testing was used and P values for all statistically significant differences ($P < 0.05$) are shown.

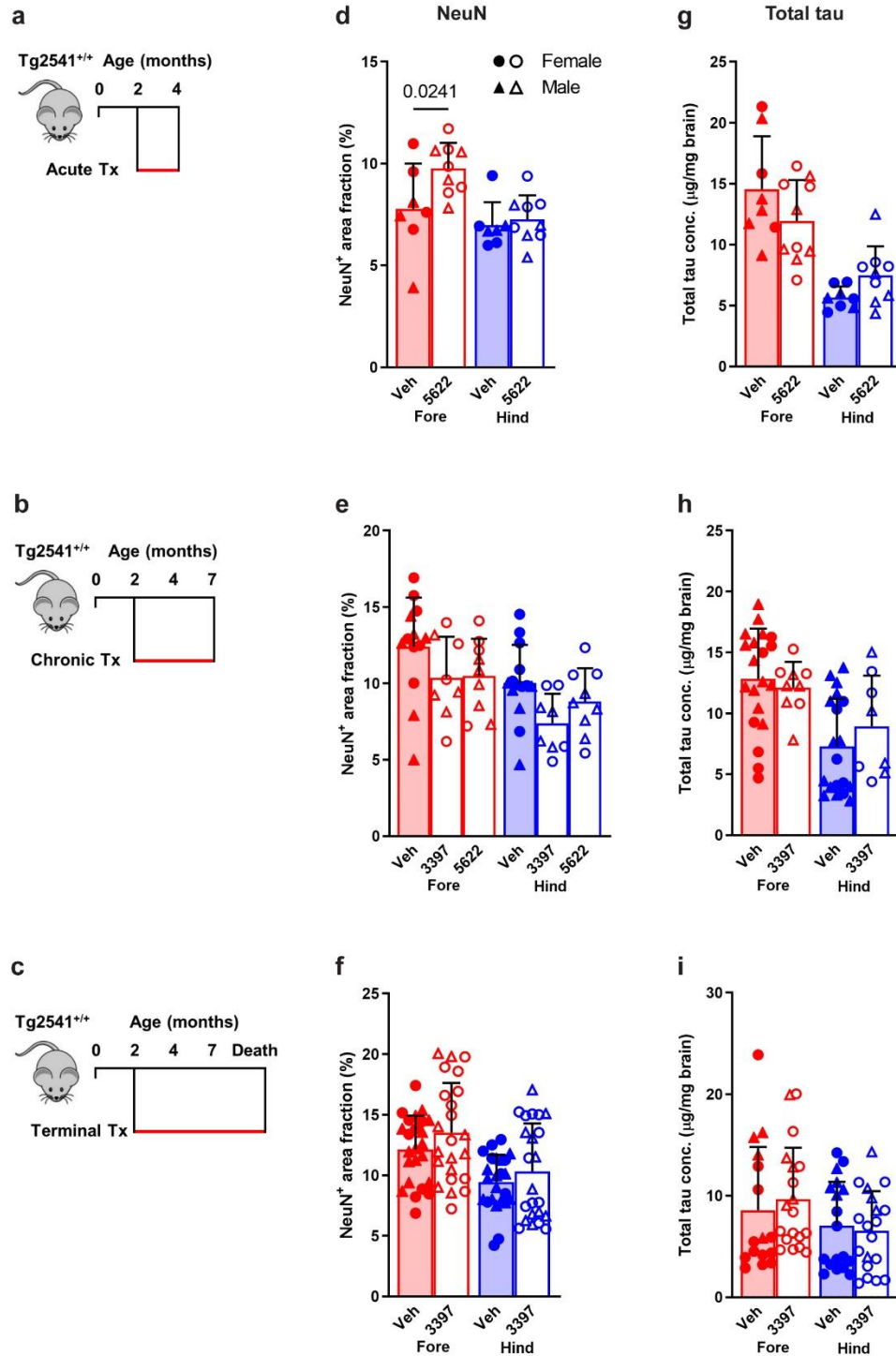


Supplementary Fig. 5| CSF1R inhibition reduces pathogenic tau spreading following K18 forebrain inoculation. **a**, Schematic of acute PLX treatment of Tg2541 mice from 2.5–4 mo of age following inoculation of K18 tau fibrils into the hippocampus and overlying cortex (forebrain regions) at 2.5 mo of age. **b**, Tau-prion levels in the ipsilateral (inoculated side) or contralateral (un-inoculated side) forebrain or hindbrain tissue homogenates of Tg2541 mice receiving acute treatment with vehicle or PLX3397 (275 mg/kg oral) following K18 forebrain inoculation, measured using the HEK293T cell tau-prion bioassay and presented as percent of cells with tau aggregates. Horizontal lines across bars indicate the mean tau-prion level in forebrain (12.54% cells with aggregates) or hindbrain (26.06% cells with aggregates) tissue homogenates of Tg2541 mice that did not undergo K18 inoculation and received acute treatment with vehicle (Un-inoc. Veh). Each symbol represents the ipsilateral or contralateral forebrain or hindbrain of an individual mouse, with female mice shown as closed or open circles and male mice shown as closed or open triangles. Error bars represent s.d. of the mean. Three-way ANOVA with Holm-Šidák post hoc testing was used and P values for all statistically significant differences ($P < 0.05$) between Veh and 3397 are shown above the bars. P values for all differences between each group and the respective brain region of Un-inoc. Veh mice are shown on the bars.



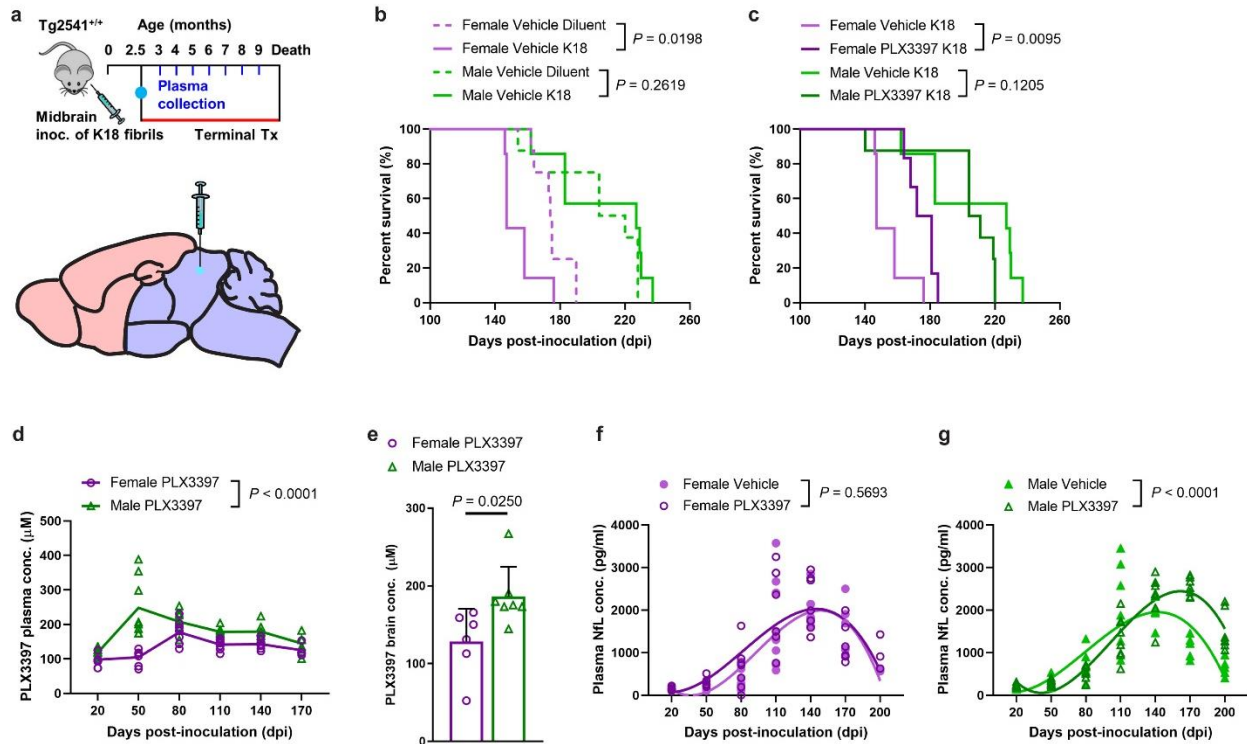
Supplementary Fig. 6 | Non-brain penetrant analog of CSF1R inhibitors does not reduce microglia or pathogenic tau levels in the brains of Tg2541 mice. **a**, Schematic of chronic treatment of Tg2541 mice from 2–7 mo of age with PLX73086, a non-brain penetrant analog of PLX3397 and PLX5622. **b,c**, Quantification of the Iba1-positive (**b**) or P2YR12-positive (**c**) area fractions by IHC in the forebrains or hindbrains of Tg2541 mice receiving chronic treatment with vehicle or PLX73086 (200 mg/kg oral). **d**, Tau-prion levels in forebrain and hindbrain tissue homogenates of Tg2541 mice receiving chronic treatment with vehicle or PLX73086, measured

using the HEK293T cell tau-prion bioassay and normalized to the vehicle group. **e,f**, Levels of pTau [S396] (**e**) or pTau [T231] (**f**) measured by ELISA in formic acid extracts of forebrain and hindbrain tissue homogenates of Tg2541 mice receiving chronic treatment with vehicle or PLX73086, normalized to total protein concentration. In **b-f**, each symbol represents the forebrain or hindbrain of an individual mouse, with female mice shown as closed or open circles and male mice shown as closed or open triangles. Error bars represent s.d. of the mean. Two-way ANOVA with Holm-Šidák post hoc testing was used and P values for all statistically significant differences ($P < 0.05$) are shown.



Supplementary Fig. 7 | CSF1R inhibition by three treatment paradigms does not affect neurons or total tau levels. a–c, Schematics of acute (a), chronic (b), or terminal (c) PLX treatment of Tg2541 mice from 2–4 mo of age, 2–7 mo of age, or 2 mo of age until death, respectively. **d–f**, Quantification of neuronal nuclei (NeuN)-positive area fraction by IHC analysis

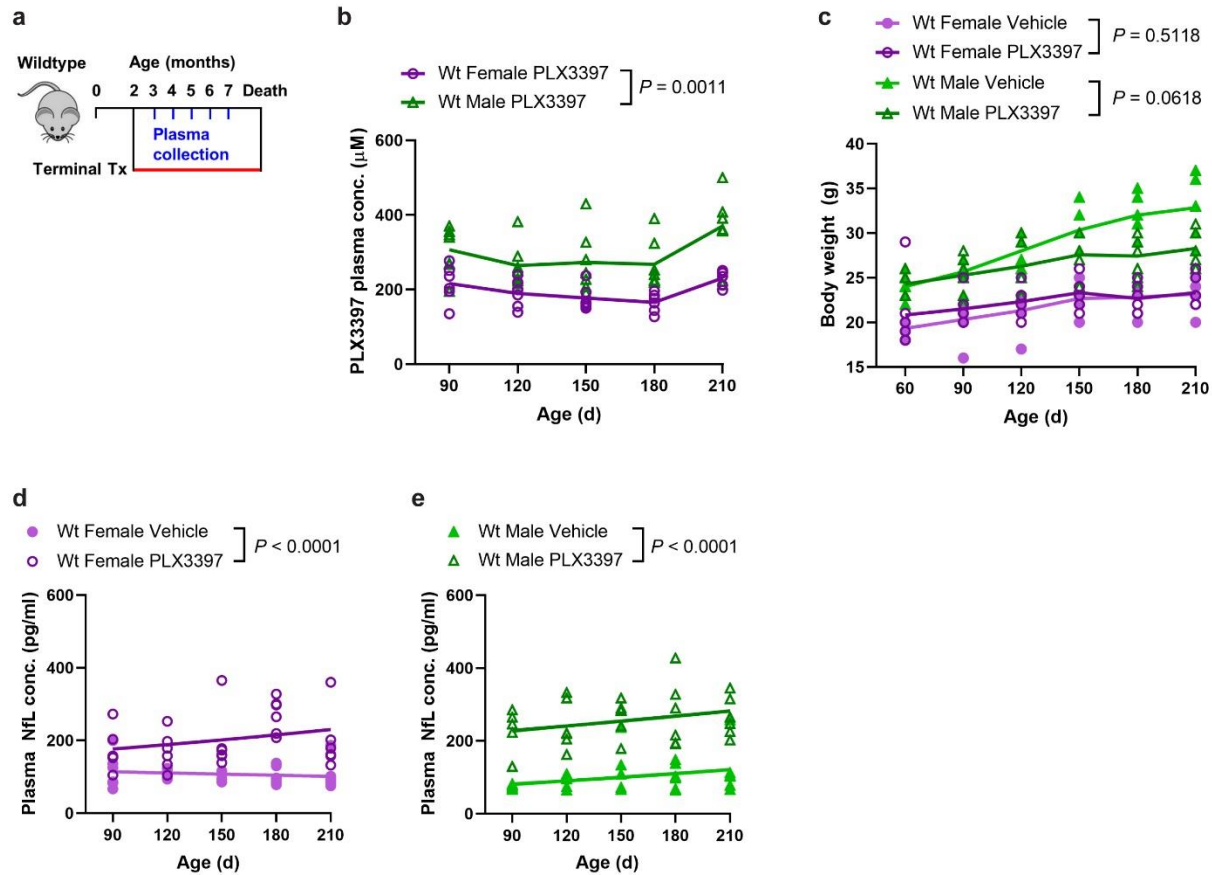
of forebrain and hindbrain areas of Tg2541 mice receiving acute (**d**), chronic (**e**), or terminal (**f**) treatment with vehicle, PLX3397 (275 mg/kg oral), or PLX5622 (1200 mg/kg oral). **g–i**, Levels of total tau measured by ELISA in forebrain and hindbrain tissue homogenates of Tg2541 mice receiving acute (**g**), chronic (**h**), or terminal treatment (**i**) with vehicle, PLX3397, or PLX5622, normalized to total protein concentration. In **d–i**, each symbol represents the forebrain or hindbrain of an individual mouse, with female mice shown as closed or open circles and male mice shown as closed or open triangles. Error bars represent s.d. of the mean. Two-way ANOVA with Holm-Šidák post hoc testing was used in **d**, and **f–i**. One-way ANOVA with Holm-Šidák post hoc testing was used in **e**. *P* values for all statistically significant differences ($P < 0.05$) are shown.



Supplementary Fig. 8| CSF1R inhibition extends survival of female mice following K18

midbrain inoculation. **a**, Schematic of terminal PLX treatment of Tg2541 mice from 2.5 mo of age until death, following inoculation of K18 tau fibrils into the midbrain (hindbrain region) at 2.5 mo of age. Blood plasma was collected at monthly intervals from 3–9 mo of age. **b**, Kaplan-Meier plot showing percent survival of female or male Tg2541 mice inoculated with K18 tau fibrils or diluent. $n=8$ mice for Female Vehicle Diluent; $n=7$ mice for Female Vehicle K18; $n=8$ mice for Male Vehicle Diluent; $n=7$ mice for Male Vehicle K18. Differences in survival between diluent and K18 inoculation in male or female mice treated with vehicle were evaluated by Log-rank (Mantel-Cox) test. **c**, Kaplan-Meier plot showing percent survival of female or male Tg2541 mice inoculated with K18 tau fibrils and then receiving terminal treatment of vehicle or PLX3397 (275 mg/kg oral). $n=7$ mice for Female Vehicle K18; $n=6$ mice for Female PLX3397 K18; $n=7$ mice for Male Vehicle K18; $n=8$ mice for Male PLX3397 K18. Differences in survival between vehicle and PLX3397 treatment in male or female mice inoculated with K18 were evaluated by Log-rank (Mantel-Cox) test. **d**, Plasma concentration of PLX3397 in female or male Tg2541 mice inoculated with K18 followed by terminal treatment with PLX3397, plotted over days post inoculation (dpi) Mixed-effects analysis (Restricted maximum likelihood) was used to compare female and male mice and the P value is shown. **e**, Brain concentration of PLX3397 at death in female or male Tg2541 mice inoculated with K18 followed by terminal treatment with PLX3397.

Error bars represent s.d. of the mean. Unpaired t test was used was used to compare female and male mice and the *P* value is shown. **f,g**, Plasma concentration of NfL in female (**f**) or male (**g**) Tg2541 mice inoculated with K18 followed by terminal treatment with vehicle or PLX3397, plotted over days post-inoculation (dpi). The differences between vehicle or PLX3397 treatments were evaluated by non-linear regression using third order polynomial models and the best-fit lines and statistical results are shown. In **d-g**, each symbol represents an individual mouse, with female mice shown as closed or open circles and male mice shown as closed or open triangles.



Supplementary Fig. 9| Plasma levels of PLX3397 and NfL, and body weights of wildtype

mice treated with CSF1R inhibitors. a, Schematic of terminal PLX treatment of C57BL/6J

wildtype mice (Wt) from 2 mo of age until death and blood plasma collected at 3, 4, 5, 6, and 7

mo of age. **b**, Plasma concentration of PLX3397 in female or male Wt mice with lines indicating

group means. The difference between female and male mice was assessed by two-way

repeated measures ANOVA. **c**, Body weights of female or male Wt mice treated with vehicle or

PLX3397 (275 mg/kg oral). Each symbol represents an individual mouse and lines indicate

group means. Differences in weight between vehicle and PLX3397 treatment in male or female

mice were evaluated by two-way repeated measures ANOVA and P values are shown. **d,e**,

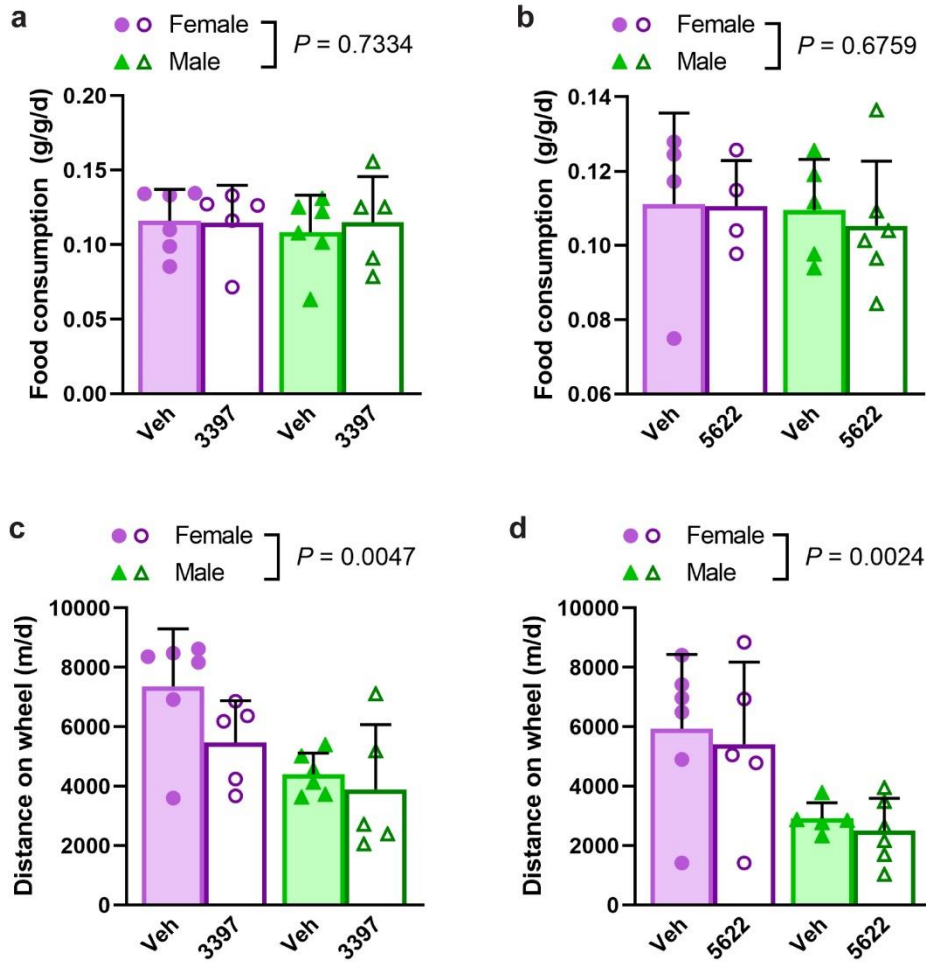
Plasma concentration of NfL in female (**d**) or male (**e**) Wt mice treated with vehicle or PLX3397.

The differences between vehicle or PLX3397 treatment were evaluated by non-linear regression

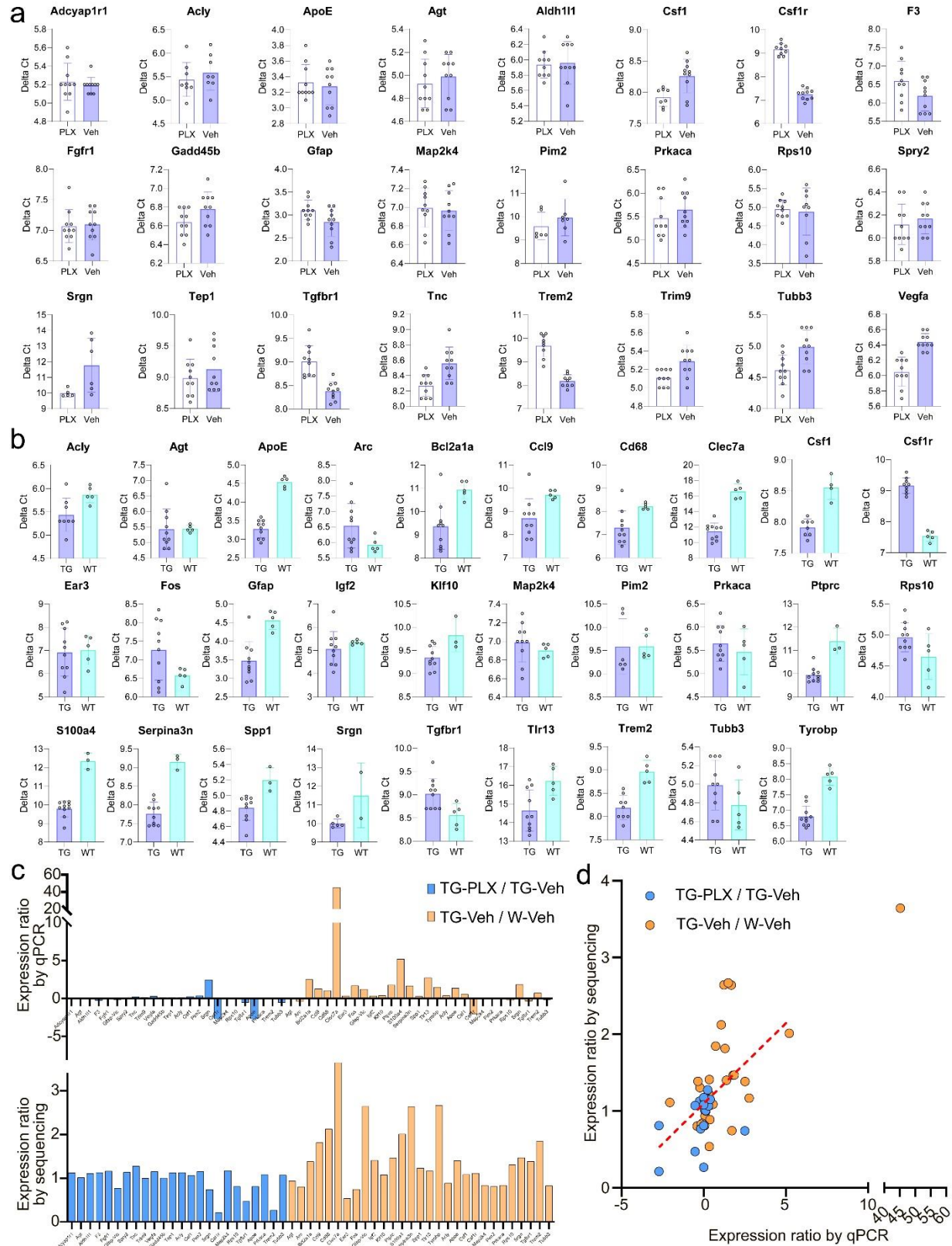
using exponential growth models and the best-fit lines and statistical results are shown. In **b-e**,

each symbol represents an individual mouse, with female mice shown as closed or open circles

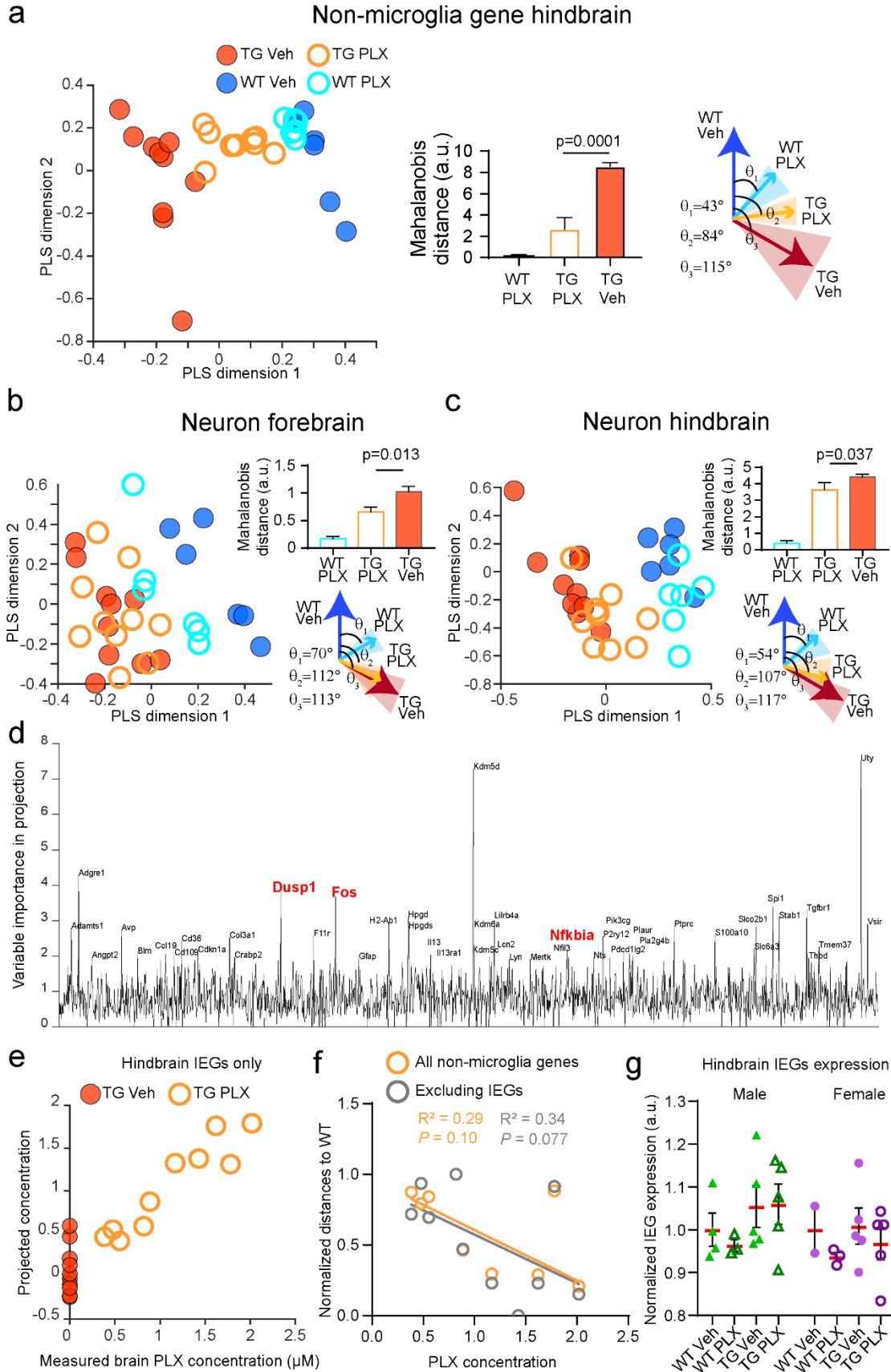
and male mice shown as closed or open triangles.



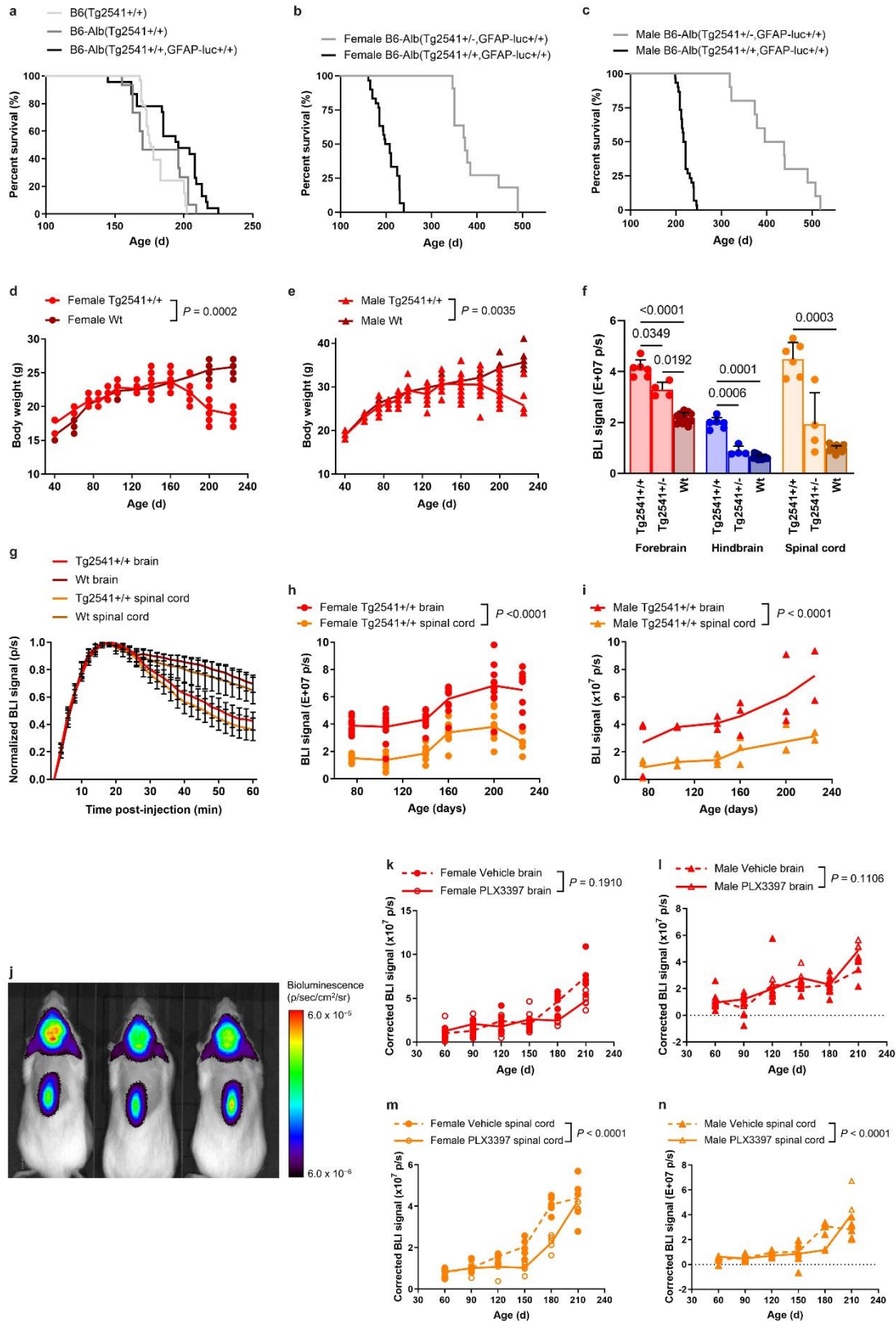
Supplementary Fig. 10| Food consumption and activity of Tg2541 mice treated with CSF1R inhibitors. **a,b**, Food consumption measured in Tg2541 mice receiving terminal treatment with vehicle or PLX3397 (275 mg/kg oral) (**a**), or vehicle or PLX5622 (1200 mg/kg oral) (**b**), reported as grams of food per gram of mouse body weight per day (g/g/d). **c,d**, Running wheel activity measured in Tg2541 mice receiving terminal treatment with vehicle or PLX3397 (**c**), or vehicle or PLX5622 (**d**), reported as total distance traveled in meters per day (m/d). In **a-d**, each symbol represents an individual mouse, with female mice shown as closed or open circles and male mice shown as closed or open triangles. Error bars represent s.d. of the mean. Two-way ANOVA was used to compare female and male mice and *P* values are shown.



a, Delta Ct values of 24 selected genes in hindbrains of Tg2541 mice treated with PLX5622 (1200 mg/kg) and vehicle. A lower Delta Ct reading indicates higher expression level. **b**, Delta Ct values of 29 selected genes in hindbrains of Tg2541 and wildtype mice treated with vehicle. A lower Delta Ct reading indicates higher expression level. **c**, Expression ratios of the 53 genes in **(a)** and **(b)** as measured by qPCR and Nanostring sequencing. **d**, Scatter plot of the data in **(c)**. Red dotted line shows a linear trend line.



Supplementary Fig. 12| Additional analyses of gene expression patterns. a–c, Analyses similar to Fig. 4, using **(a)** all non-microglia genes in hindbrain, or neuron-specific genes in **(b)** forebrain and **(c)** hindbrain. **d–g**, Analyses similar to Fig. 4g–j, using data from hindbrains.



Supplementary Fig. 13| Generation, validation and optimization of bigenic Tg2541 mice

for in vivo bioluminescent imaging of astrocytosis. **a**, Kaplan-Meier plot shows that the survival curve (kinetics of disease) is unchanged for Tg2541 homozygous mice bred to B6-albino background and homozygous for the reporter GFAP-luciferase transgene. **b, c**, Kaplan-Meier plots for **(b)** female and **(c)** male mice showing that survival curves of homozygous and hemizygous B6-albino bigenic Tg2541 mice is not sex-dependent; homozygous Tg2541 mice have a median survival of 212 days, and hemizygous Tg2541 mice have a median survival of 378 days. **d,e**, As a crude surrogate of general health, longitudinal measurements of mouse body weight (grams) shows that in contrast to Wt mice, **(d)** female and **(e)** male Tg2541 mice lose weight as a result of decreased food intake from increasing paraparesis with disease progression. Because earlier studies gave a standard volume of d-luciferin substrate regardless of changes in individual mouse weight, we optimized the protocol to give a 25mg/kg of CycLuc1 to increase consistency in BLI measurements. **f**, To validate the GFAP-luciferase reporter gene and the synthetic luciferin substrate (CycLuc1) *in vivo*, we performed BLI in Tg2541 homozygous mice (~200 days old) with advanced disease pathology and showed the BLI signal is significantly increased in the forebrain, hindbrain and spinal cord as compared to similar aged Tg2541 hemizygous and Wt mice. **g**, Time-lapse imaging (two-minute intervals) of BLI signal from brain and spinal cord in Tg and Wt mice showed that peak BLI signal occurred between 14 and 20 minutes after CycLuc1 injection to the peritoneum. Thus, to decrease variability in our study, we collect images at 14, 16, and 18 minutes post-injection and average all three time points to account for subtle differences in time of injection and individual mouse pharmacokinetic of CycLuc1. **h,i**, Longitudinal BLI plots in **(h)** female and **(i)** male mice show kinetics of gliosis in the Tg2541 brain and spinal cord (3 mice per field of view). **j**, Example image of the field of view (magnification) used to capture both the brain and spinal cord in three mice per time point. **k,l**, Longitudinal BLI plots in **(k)** female and **(l)** male mice treated with PLX3397 (275 mg/kg oral) or vehicle. Due to resolution and/or sensitivity of this magnification, differences between groups were not measured. Zoomed imaging on single mice from the same cohort was performed as shown in Figure 4. **m,n**, BLI plots show suppression of BLI signal in the spinal cords of PLX3397-treated **(m)** female and **(n)** male Tg2541 mice compared to vehicle-treated Tg2541 mice.

Supplementary Table 1 | Statistical analysis of sex-specific effect.

Panel	Measure	Experiment	P-value
Fig. 1e	Cell assay	Acute	0.0010
Fig. 1f	Cell assay	Chronic	0.0427
Fig. 1g	Cell assay	Terminal	0.0006
Fig. 1h	pS396	Acute	0.0591
Fig. 1i	pS396	Chronic	0.5733
Fig. 1j	pS396	Terminal	0.9602
Fig. 1k	pS202/T205	Acute	0.4847
Fig. 1l	pS202/T205	Chronic	0.2522
Fig. 1m	pS202/T205	Terminal	0.3689
Fig. S1e	Iba1	Acute	0.3078
Fig. S1f	Iba1	Terminal	0.0259
Fig. S1g	Iba1	Chronic	0.2012
Fig. S1h	P2YR12	Acute	0.0693
Fig. S1i	P2YR12	Terminal	0.0367
Fig. S1j	P2YR12	Chronic	0.0400
Fig. S1m	Iba1	Acute (Wt)	0.0351
Fig. S1n	Iba1	Terminal (Wt)	0.0732
Fig. S1o	P2YR12	Acute (Wt)	0.1630
Fig. S1p	P2YR12	Terminal (Wt)	0.5502
Fig. S2e	Cell assay	Tg vs. Wt	0.8069
Fig. S3b	Iba1	Spinal cord	0.2063
Fig. S3c	Cell assay	Spinal cord	0.0017
Fig. S3d	pS202/T205	Spinal cord	0.3597
Fig. S4b	Cell assay	Interventional	0.0363
Fig. S4c	pS396	Interventional	0.5403
Fig. S4d	pT231	Interventional	0.1298
Fig. S4f	Iba1	Intermittent	0.3434
Fig. S4g	P2YR12	Intermittent	0.9212
Fig. S4h	Cell assay	Intermittent	0.0684
Fig. S4i	pT231	Intermittent	0.8818
Fig. S5b	Cell assay	Forebrain inoculation	0.0149
Fig. S6b	Iba1	PLX-73086	0.0218
Fig. S6c	P2YR12	PLX-73086	0.9773
Fig. S6d	Cell assay	PLX-73086	0.2758
Fig. S6e	pS396	PLX-73086	0.5043
Fig. S6f	pT231	PLX-73086	0.2062
Fig. S7d	NeuN	Acute	0.0648
Fig. S7e	NeuN	Chronic	0.0183
Fig. S7f	NeuN	Terminal	0.5458
Fig. S7g	Total tau	Acute	0.2494
Fig. S7h	Total tau	Chronic	0.4865
Fig. S7i	Total tau	Terminal	0.8885